Pore-scale modeling of phase change in porous media

Luis Cueto-Felgueroso,[1,*] Xiaojing Fu,[2] and Ruben Juanes[2]
[1]*Universidad Politécnica de Madrid, Calle del Profesor Aranguren 3, 28040 Madrid, Spain*
[2]*Massachusetts Institute of Technology, 77 Massachusetts Avenue, Cambridge, Massachusetts 02139, USA*

(Received 12 July 2017; published 8 August 2018)

The combination of high-resolution visualization techniques and pore-scale flow modeling is a powerful tool used to understand multiphase flow mechanisms in porous media and their impact on reservoir-scale processes. One of the main open challenges in pore-scale modeling is the direct simulation of flows involving multicomponent mixtures with complex phase behavior. Reservoir fluid mixtures are often described through cubic equations of state, which makes diffuse-interface, or phase-field, theories particularly appealing as a modeling framework. What is still unclear is whether equation-of-state-driven diffuse-interface models can adequately describe processes where surface tension and wetting phenomena play important roles. Here we present a diffuse-interface model of single-component two-phase flow (a van der Waals fluid) in a porous medium under different wetting conditions. We propose a simplified Darcy-Korteweg model that is appropriate to describe flow in a Hele-Shaw cell or a micromodel, with a gap-averaged velocity. We study the ability of the diffuse-interface model to capture capillary pressure and the dynamics of vaporization-condensation fronts and show that the model reproduces pressure fluctuations that emerge from abrupt interface displacements (Haines jumps) and from the breakup of wetting films.

DOI: 10.1103/PhysRevFluids.3.084302

I. INTRODUCTION

The emergence of imaging techniques capable of producing three-dimensional representations of the pore space of rocks has led to the rapid development of pore-scale modeling as a predictive tool in the oil and gas industry and the geosciences [1]. Model predictions made directly on images of small rock samples may provide data that would be much more difficult to obtain using traditional experimental methods [2–4]. The full potential of pore-scale simulation can only be realized if models of increasing accuracy honoring both the multiphase flow dynamics and the rock geometry are available.

Popular approaches for the direct simulation of immiscible flow in the pore space inferred from three-dimensional images include the lattice Boltzmann method [5–10], the volume-of-fluid method [11–15], which solves the Navier-Stokes equations together with a relatively straightforward advection and reconstruction of fluid-fluid interfaces, and the level set method [16–18]. Pore-scale modeling based on diffuse-interface, or phase-field, modeling is emerging as a promising alternative to traditional approaches. The use of diffuse-interface models to describe interfacial phenomena originated in the early works of Gibbs, Korteweg, and Cahn and Hilliard, together with the Landau-Ginzburg mean-field theory of phase transitions [19–21]. The fundamental idea of tracking and properly capturing interface dynamics through phase-field theories was subsequently generalized and adapted to multiphase fluid flow scenarios [22]. While variational or thermodynamic

*luis.cueto@upm.es

theories are perhaps the most common theoretical framework to rigorously derive these models [22–34], diffuse-interface theories have been obtained from averaging microscale interactions [35] or rationalized as a microforce balance [36]. The common goal in these approaches is to formulate thermodynamically consistent stress tensors and mesoscale balance laws, including the impact of surface tension on the momentum balance, as well as properly tracking interfacial dynamics [25]. Pore-scale modeling of immiscible two-phase flow using phase-field models has been done in [37–39]. We have successfully used the phase-field modeling framework to describe wetting and capillary phenomena in porous media, from unsaturated flow [40], thin films, and partial wetting [41,42] to pattern formation during immiscible displacement in Hele-Shaw flow [43].

While essential to understanding many practical applications in engineering and the geosciences, multicomponent flows with complex phase behavior remain largely unexplored in pore-scale modeling. Darcy-scale general purpose simulators assume local thermodynamic equilibrium [44–46] and perform equation-of-state-based calculations to determine phase equilibrium predictions, that is, determine the phase volume fractions and their compositions from overall component mole fractions [47,48]. Whether the thermodynamic equilibrium assumption is warranted at the Darcy scale, given the flow conditions, complex structure of the pore space, and characteristic timescales for flow, is a fundamental open question in reservoir simulation. The simplest case is that of a single-component liquid-vapor system. While retaining many of the essential elements of nonequilibrium phase behavior that are needed to understand more general multicomponent systems, rigorous thermomechanical models for liquid-vapor systems are easier to derive and discretize in complex geometries.

Simulations of liquid-vapor flows have been carried out with lattice-gas models [49,50], also in porous media [51,52], and more recently with lattice-Boltzmann methods [53–56], and with smoothed particle hydrodynamics [57]. As the continuum thermomechanical theory of a van der Waals fluid, the Navier-Stokes-Korteweg (NSK) equations [58] represent perhaps the earliest of diffuse-interface models, describing the dynamics of a single-component two-phase system. Simulations of liquid-vapor flow using the NSK model have been performed, with a focus on bulk processes (boiling and cavitation), in [59–70], and on the interaction with solids to model phase-change-driven implosion [71]. Phase separation in liquid-vapor systems with other cubic equations of state has been simulated by [72–75].

Here we present simulations of pore-scale liquid-vapor flow processes of a van der Waals fluid using the Navier-Stokes-Korteweg diffuse-interface model. We simplify the hydrodynamics by proposing a Darcy-Korteweg model to describe liquid-vapor flows in Hele-Shaw cells or micromodels. We study the impact of wetting conditions and pore space geometry on phase ordering dynamics. A supercritical homogeneous fluid that is rapidly quenched below the critical temperature into the unstable region will undergo spinodal decomposition. After the initial separation phase the pore domains occupied by the different phases will grow in a coarsening process that evolves towards the minimization of interfacial energy. In the bulk, the scaling regimes that ensue at long times are relatively well understood [21], although hydrodynamic instabilities may arrest the classical coarsening process [76].

The problem of liquid-vapor transitions in porous media with different wetting conditions, however, remains largely unexplored. The practical relevance of these phase ordering processes lies in the fact that they may control the initial distribution of fluids within the pore space, as well as phase connectivity. Phase connectivity is directly linked to phase mobility, while fluid-fluid interfacial areas control mass and heat transfer and equilibrium capillary pressures.

We also evaluate the challenges of direct simulation, at the pore scale, of fluids and fluid mixtures described by equations of state. As pointed out in [59], the effective surface tension in the NSK diffuse-interface model increases with the interface width, which would need to be artificially enlarged to resolve flows beyond the micrometer scale. This error in surface tension is currently a key open issue in the application of this approach to millimeter-scale simulations.

We also study the dynamics of vaporization and condensation fronts under different wetting conditions. In particular, we show that the diffuse-interface model is able to capture pressure fluctuations

generated as liquid-vapor interfaces advance, in accordance with experimental observations [77–82]. We also conclude that phase-change fronts are controlled by heterogeneity, a feature that is typical of evaporation fronts, interpreted as modified invasion percolation processes [83–87].

II. THE NAVIER-STOKES-KORTEWEG MODEL AS A DIFFUSE-INTERFACE MODEL

The starting point for our model is the compressible, isothermal Navier-Stokes equations with Korteweg stresses, describing the flow of a two-phase single-component system [58,61,65]

$$\frac{\partial \rho}{\partial t} + \nabla \cdot (\rho \mathbf{u}) = 0, \tag{1}$$

$$\frac{\partial (\rho \mathbf{u})}{\partial t} + \nabla \cdot (\rho \mathbf{u} \otimes \mathbf{u} + p\mathbf{I}) - \nabla \cdot \tau - \nabla \cdot \kappa = \rho \mathbf{b}, \tag{2}$$

where $\rho \mathbf{b}$ is the body force, and the viscous shear stress and Korteweg stress τ and κ respectively, are given by

$$\tau = \mu(\nabla \mathbf{u} + \nabla^T \mathbf{u}) + \xi(\nabla \cdot \mathbf{u})\mathbf{I} \tag{3}$$

and

$$\kappa = \lambda\big(\rho \nabla^2 \rho + \tfrac{1}{2}|\nabla \rho|^2\big)\mathbf{I} - \lambda \nabla \rho \otimes \nabla \rho, \tag{4}$$

where μ and ξ are the shear and bulk viscosity coefficients and λ is the capillary coefficient. For constant λ, the capillary force contribution to the momentum equation reduces to

$$\nabla \cdot \kappa = \lambda \rho \nabla (\nabla^2 \rho). \tag{5}$$

The field equations (1)–(4) are supplemented with a suitable equation of state, relating fluid pressure, density, and temperature, $p \equiv p(\rho, T)$. The key insight in the van der Waals theory of fluids is that phase coexistence and phase transitions may be modeled through a nonmonotonic pressure-density relation. In turn, this nonmonotonic behavior requires a regularization mechanism to provide the structure of the interface. In the above model, such regularization is introduced by the Korteweg stresses (4) and (5). The capillary terms may be understood as arising from a generalization of the fluid free energy and other thermodynamic quantities, in the sense that the free energy is not only a function of density and temperature, but also a function of the norm of the density gradient $\frac{1}{2}|\nabla \rho|^2$ as

$$\psi_\nabla(\rho, T, |\nabla \rho|^2) = R\psi(\rho, T) + \frac{\lambda}{2\rho}|\nabla \rho|^2, \tag{6}$$

where $\psi(\rho, T)$ is the bulk free-energy density of the fluid, consistent with the particular equation-of-state model. Surface tension in the Navier-Stokes-Korteweg model increases with the strength of the gradient energy term, as

$$\sigma \sim \sqrt{\lambda}, \tag{7}$$

with proportionality constant

$$c_0 = \sqrt{2} \int_{\rho_v^M}^{\rho_l^M} \sqrt{\rho \psi(\rho) - \rho \nu\big(\rho_v^M\big) + p\big(\rho_v^M\big)} d\rho. \tag{8}$$

The interface width also scales with the square root of λ,

$$\delta(T, \lambda) \sim T^2 \sqrt{\lambda}. \tag{9}$$

A. Equation of state: van der Waals fluid

For simplicity, in this study we will adopt the van der Waals equation of state, which is a correction of the ideal gas law to account for real-gas effects,

$$\left(p + \frac{a}{v^2}\right)(v - b) = RT \tag{10}$$

or

$$p = \frac{RT}{v - b} - \frac{a}{v^2}, \tag{11}$$

where p is the pressure, T is the temperature, v is the molar volume, R is the specific gas constant, and a and b are model parameters that characterize a particular substance. For convenience in coupling the equation of state with the field equations (1) and (2), we write the above equation of state in terms of density $\rho = 1/v$ (mol/m^3) as

$$p(\rho, T) = Rb^* \frac{\rho T}{b^* - \rho} - a\rho^2, \tag{12}$$

where $b^* = 1/b$. We will work with reduced quantities, normalized with respect to those of the critical point. The critical temperature T_c, pressure p_c, and density ρ_c in the van der Waals model are given by

$$T_c = \frac{8ab^*}{27R}, \quad p_c = \frac{ab^{*2}}{27}, \quad \rho_c = \frac{b^*}{3}, \tag{13}$$

leading to a critical compressibility factor

$$Z_c = \frac{p_c v_c}{RT_c} = \frac{3}{8}. \tag{14}$$

Written in terms of reduced variables $p_r = p/p_c$, $\rho_r = \rho/\rho_c$, and $T_r = T/T_c$, the equation of state becomes

$$p_r = \frac{8T_r\rho_r}{3 - \rho_r} - 3\rho_r^2. \tag{15}$$

It is useful to identify the Helmholtz free-energy density ψ, which is the bulk free-energy density in Eq. (6), such that $p = \rho^2 \partial\psi/\partial\rho$, as

$$\psi(\rho, T) = -a\rho + RT \log \frac{\rho}{b^* - \rho} - C_v T\left(\log \frac{T}{T_0} - 1\right), \tag{16}$$

where C_v is the specific-heat capacity at constant volume. In reduced quantities,

$$\psi_r(\rho_r, T_r) = -3\rho_r + \frac{8}{3}T_r \log \frac{\rho_r}{3 - \rho_r} - c_v T_r\left(\log \frac{T_r}{T_{0r}} - 1\right). \tag{17}$$

The chemical potential ν, defined as $\nu = \partial(\rho\psi)/\partial\rho$, is given by

$$\nu(\rho, T) = -2a\rho + RT\left(\frac{b^*}{b^* - \rho} + \log \frac{\rho}{b^* - \rho}\right) - C_v T\left(\log \frac{T}{T_0} - 1\right) \tag{18}$$

or, in reduced quantities,

$$\nu_r(\rho_r, T_r) = -6\rho_r + \frac{8}{3}T_r\left(\frac{3}{3 - \rho_r} + \log \frac{\rho_r}{3 - \rho_r}\right) - c_v T_r\left(\log \frac{T_r}{T_{0r}} - 1\right). \tag{19}$$

An important feature of van der Waals–type equations of state is the presence of a nonmonotonic pressure-density relationship or, equivalently, a nonconvex free energy (Fig. 1). Inside this nonconvex spinodal region, a homogeneous system is mechanically unstable under infinitesimal perturbations, as pressure decreases with increasing density, which induces phase separation.

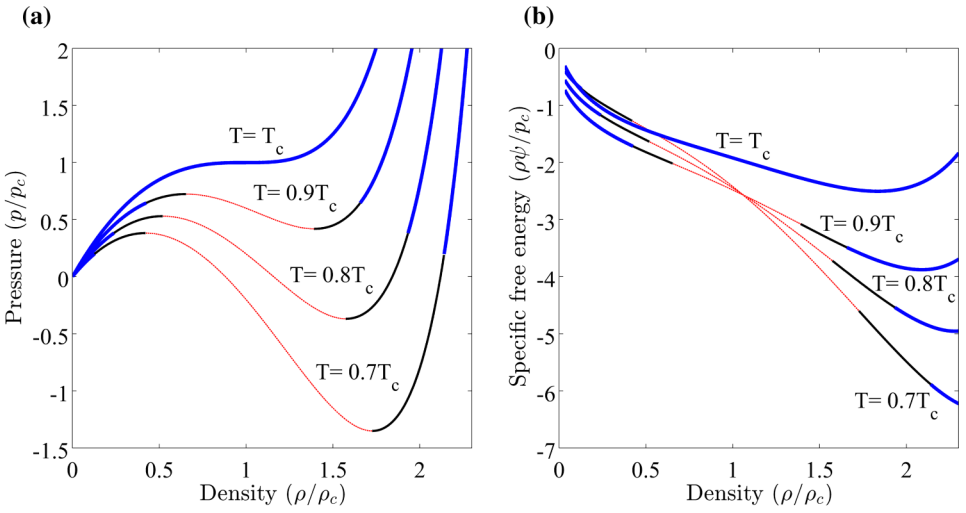

FIG. 1. The van der Waals equation of state near the critical point. (a) Pressure isotherms as a function of density at various temperatures. Below the critical temperature the pressure is nonmonotonic, which reveals the presence of an unstable region that leads to phase separation and phase coexistence. In these pressure isotherms we indicate stable (blue line), metastable (black line), and unstable (red line) regions. (b) The Helmholtz free energy is nonconvex below the critical temperature, with a concave region that corresponds to the unstable region promoting spinodal decomposition. We use the same color code for stable, metastable, and unstable regions.

B. Cubic equations of state as improvements over the van der Waals model

The formulation and analysis presented here are rather general and can be applied to other equations of state. In particular, reservoir fluids are usually modeled through cubic equations of state of the general form [47]

$$p = \frac{RT}{v-b} - \frac{a(T)}{(v+\delta_1 b)(v+\delta_2 b)}, \tag{20}$$

with compressibility factor

$$Z\left(\frac{b}{v}, \frac{a(T)}{RTb}\right) = \frac{1}{1-b/v} - \frac{a(T)}{RTb}\frac{b/v}{(1+\delta_1 b/v)(1+\delta_2 b/v)}. \tag{21}$$

In the above framework, the van der Waals equation of state corresponds to $\delta_1 = 0$, $\delta_2 = 0$, and constant $a(T)$. The Soave-Redlich-Kwong (SRK) equation corresponds to $\delta_1 = 1$ and $\delta_2 = 0$, and the Peng-Robinson (PR) equation is recovered when $\delta_1 = 1 + \sqrt{2}$ and $\delta_2 = 1 - \sqrt{2}$. The parameters a and b in the SRK and PR equations of state are functions of temperature and other substance properties [47].

C. Liquid-vapor equilibrium and Maxwell states

The existence of a spinodal region in the equation of state implies that two phases may coexist at temperatures below the critical temperature. The liquid and vapor phases must be energetically and mechanically stable at equilibrium. When separated by a flat interface, their densities satisfy the relationships

$$p\left(T, \rho_v^M\right) = p\left(T, \rho_l^M\right), \tag{22}$$

$$v\left(T, \rho_v^M\right) = v\left(T, \rho_l^M\right), \tag{23}$$

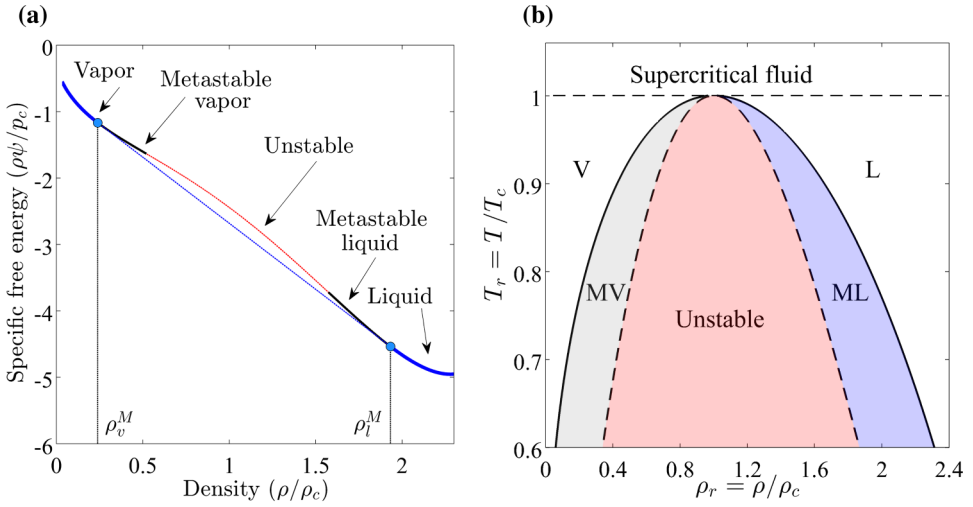

FIG. 2. Phase equilibrium and phase diagram for a van der Waals fluid. (a) At a given temperature, states with homogeneous density are only possible at sufficiently large (liquid) or small (vapor) densities (blue lines). Densities lying inside the spinodal region (red line) are unstable, leading to phase separation. The equilibrium vapor and liquid densities in heterogeneous states, where liquid and vapor coexist, are obtained through the common-tangent construction in the specific free energy. The equilibrium states are commonly known as Maxwell states ρ_l^M and ρ_v^M. The convex regions between the unstable region and the Maxwell states are metastable (black lines). (b) Phase diagram for a van der Waals fluid at different temperatures and average density. The shaded areas indicate metastable vapor (MV), metastable liquid (ML), and unstable states.

where the superscript M refers to thermodynamic equilibria, or Maxwell states, which can be seen as equilibrium values at constant temperature. The graphical interpretation of this condition is Maxwell's equal area rule, or tangent construction in the free energy, that is, in the ρ-$\rho\psi$ plot [Fig. 2(a)]. The common tangent line passing through the Maxwell states lies below the energy curve, demonstrating that the two-phase state is favored over the homogeneous state. The locus of Maxwell states at different temperature corresponds to the binodal line in the phase diagram, while the locus of inflection points of $\rho\psi$ is the spinodal line, marking the transition between the unstable region and the metastable states [Fig. 2(b)]. Metastable states are physically accessible but energetically unstable, and perturbations may drive the system towards the two-phase state [25].

D. Minimal model for pore-scale simulations: Isothermal Darcy-Korteweg flow

In the following we will concentrate on a simplified hydrodynamic model, which describes flow in a Hele-Shaw cell or micromodel, which is often used as an analogous system to study porous media flow. Neglecting inertia and assuming that viscous forces are proportional to the gap-integrated fluid velocity, the momentum equation (2) reduces to a Darcy-type volumetric flux

$$\mathbf{u} = -\frac{k}{\mu}[\nabla p - \rho\mathbf{g} - \lambda\rho\nabla(\nabla^2\rho)], \tag{24}$$

which implies the lubrication approximation, with permeability $k = h^2/12$,

$$\nabla\cdot\boldsymbol{\tau} = -\frac{12\mu}{h^2}\mathbf{u}. \tag{25}$$

where h is the gap thickness.

Using the above Darcy flow model, conservation of mass reads

$$\frac{\partial \rho}{\partial t} + \nabla \cdot \left[-\rho \frac{h^2}{12\mu} [\nabla p - \rho \mathbf{g} - \lambda \rho \nabla (\nabla^2 \rho)] \right] = 0, \tag{26}$$

where the thermodynamic pressure is

$$p(\rho) = Rb^* \frac{\rho T}{b^* - \rho} - a\rho^2, \tag{27}$$

and we assume that the temperature T is constant. At the solid walls inside the micromodel we impose the static contact angle θ as [88]

$$-\frac{\nabla \rho}{|\nabla \rho|} \cdot \mathbf{n} = \cos\theta. \tag{28}$$

The mathematical structure of the above model is basically identical to that of the Hele-Shaw flow model proposed in [89]. The key difference in the present formulation is that pressure is thermodynamic, describing the liquid-vapor phase transition, rather than being derived from a synthetic double-well potential. In dimensionless quantities, using the critical pressure and density as reference values p_c and ρ_c, respectively, and the characteristic domain size L as reference length, the model equation reduces to

$$\begin{aligned} &\frac{\partial \rho_r}{\partial t} + \nabla \cdot \left[-\frac{\rho_r}{\mu_r} [\nabla p_r - \Lambda \rho_r \nabla (\nabla^2 \rho_r)] \right] = 0, \\ &p_r = \frac{8 T_r \rho_r}{3 - \rho_r} - 3\rho_r^2, \end{aligned} \tag{29}$$

where $\rho_r = \rho/\rho_c$ and $p_r = p/p_c$ are the reduced density and pressure, respectively, and time has been rescaled $t = t_D t^*$, using the characteristic time

$$t^* = \frac{12 L^2 \mu_0}{h^2 p_c}, \tag{30}$$

and we defined the Korteweg number Λ as

$$\Lambda = \frac{\lambda \rho_c^2 p_c}{L}. \tag{31}$$

The dimensionless surface tension $\sigma_D = \frac{\sigma}{p_c L}$ is expected to scale as $\sigma_D \sim \sqrt{\Lambda}$. For fixed substance properties (p_c and ρ_c) and domain size L, this scaling implies that surface tension changes with the thickness of the interface, which is in principle a computational parameter.

In the present isothermal case, we adopt a simple density-dependent viscosity model. In dimensionless form, the viscosity law is given by

$$\mu_r \equiv \mu_r(\rho_r) = \mu_{r0} \exp A\rho_r. \tag{32}$$

In the simulations below we set $\mu_{r0} = 0.005$ and $A = 3$, so the viscosity contrast between liquid and vapor is around 500 at $T_r = 0.7$.

E. Mixed formulation and finite-element discretization

We solve the model (29) using C^0 continuous finite elements and standard Bubnov-Galerkin weighting. We adopt a mixed formulation where we exploit the identity

$$\frac{\partial p}{\partial \rho} = 2\rho \frac{\partial \psi}{\partial \rho} + \rho^2 \frac{\partial^2 \psi}{\partial \rho^2} = \rho \frac{\partial \nu}{\partial \rho}, \tag{33}$$

which implies, under isothermal conditions,

$$\nabla p = \rho \nabla v. \tag{34}$$

The above transformation yields a straightforward split of the fourth-order equation (29) into a set of two second-order equations

$$\frac{\partial \rho_r}{\partial t} + \nabla \cdot \left(-\frac{\rho_r^2}{\mu_r(\rho_r)} \nabla \Pi \right) = 0, \tag{35}$$

$$\Pi = \nu_r - \Lambda \nabla^2 \rho_r, \tag{36}$$

where the dimensionless chemical potential ν_r is

$$\nu_r(\rho_r) = -6\rho_r + \frac{8}{3} T_r \left(\frac{3}{3-\rho_r} + \log \frac{\rho_r}{3-\rho_r} \right) - c_v T_r \left(\log \frac{T_r}{T_{0r}} - 1 \right). \tag{37}$$

The strong form of the problem (36) and (37) is supplemented with Dirichlet boundary conditions, as well as the contact angle at the impermeable solid walls:

$$-\Lambda \nabla \rho_r \cdot \mathbf{n} = \Lambda |\nabla \rho_r| \cos\theta, \quad \nabla \Pi \cdot \mathbf{n} = 0.$$

The weak form of the problem, with test and trial functions chosen from suitable functional spaces, can be stated as follows: Find approximations to ρ_r and Π, $\tilde{\rho}$ and $\tilde{\Pi}$, that satisfy the Dirichlet boundary conditions and are such that, for all ω and χ,

$$\int_\Omega \omega \frac{\partial \tilde{\rho}}{\partial t} d\Omega + \int_\Omega \nabla \omega \cdot \left(\frac{\tilde{\rho}^2}{\mu_r(\tilde{\rho})} \nabla \tilde{\Pi} \right) d\Omega$$
$$+ \int_\Omega \chi (\nu_r(\tilde{\rho}) - \tilde{\Pi}) \Omega + \int_\Omega \nabla \chi \cdot (\Lambda \nabla \tilde{\rho}) d\Omega + \int_\Gamma \chi \Lambda |\nabla \rho_r| \cos\theta \, d\Gamma = 0.$$

To arrive at the fully discrete model, we use unstructured triangular meshes with piecewise linear shape functions and a second-order backward differentiation formula for time integration.

III. MODEL VALIDATION: TESTING THE YOUNG-LAPLACE CAPILLARY PRESSURE

As a validation test of the two-phase model with wetting (26)–(28), we begin by simulating a liquid bridge at equilibrium in a two-dimensional channel (Figs. 3–6). We set a reduced temperature $T_r = 0.7$ and initialize the system as a liquid slug whose shape relaxes to a steady-state configuration that is controlled by the static contact angle θ and Korteweg number Λ. The domain size is 4×1 in dimensionless units. We impose no-flow boundary conditions at all walls so that pressures are constant in the bulk vapor and liquid phases away from the interface. Surface tension and the wetting conditions lead to different pressures in the vapor and liquid phases at steady state (Fig. 3). In particular, the reduced liquid and vapor pressures p_{rv} and p_{rl}, respectively, must satisfy the Young-Laplace equation which, in the present case of a two-dimensional channel, reads

$$\Delta p_r = p_{rv} - p_{rl} = \frac{\sigma \cos\theta}{H/2}, \tag{38}$$

where H is the channel width and σ is the surface tension. As a first validation, we test the linear relationship between Δp_r and $\cos\theta$ for a given channel geometry ($H = 1$) and interface thickness (through the Korteweg number $\Lambda = 10^{-4}$). The linear trend observed in the simulations indicates that the diffuse-interface model honors the Young-Laplace equation (Fig. 4). Note that the pressure shown in Fig. 4 is not the thermodynamic pressure p_r but the functional $\widetilde{p}_r = p_r - \rho_r \Lambda \nabla^2 \rho_r + \Lambda/2 |\nabla \rho_r|^2$, which includes contributions from the Korteweg stresses at the interface and yields a nearly monotonic transition between vapor and fluid.

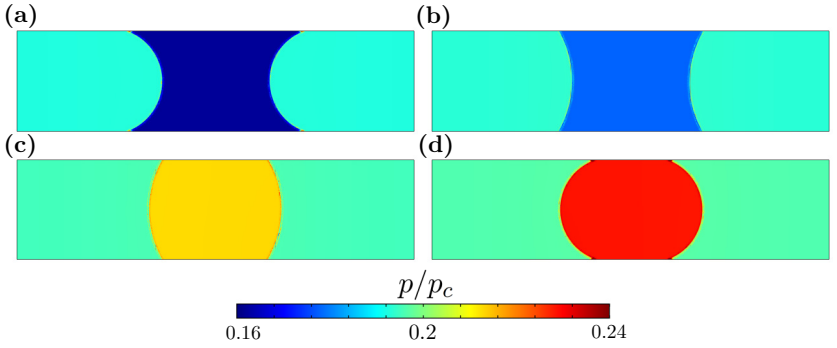

FIG. 3. Model validation using the Young-Laplace equation for a liquid slug: pressure maps. We compute the equilibrium density field for a liquid bridge in a microchannel. We vary the static contact angle (a) $\theta = 30^\circ$, (b) $\theta = 60^\circ$, (c) $\theta = 120^\circ$, and (d) $\theta = 150^\circ$. The initial condition is such that the liquid bridge occupies the center of the domain at equilibrium. When the liquid phase is wetting ($\theta < 90^\circ$), the pressure inside the slug is lower than that of the surrounding vapor. Otherwise, the pressure inside the liquid bridge is larger than the pressure of the vapor.

A. Scaling of effective surface tension with the numerical interface width

An important phenomenon in the direct numerical simulation of multiphase flow using equations of state (EOSs) is the emergence of a scale-dependent surface tension, that is, the effective surface tension depends on the interface thickness. In practice, this interface width is a numerical parameter, the smallest that can be resolved with affordable computational grids. This issue was studied in detail by Jamet *et al.* [59] and remains an open challenge that restricts the direct application of EOS-based

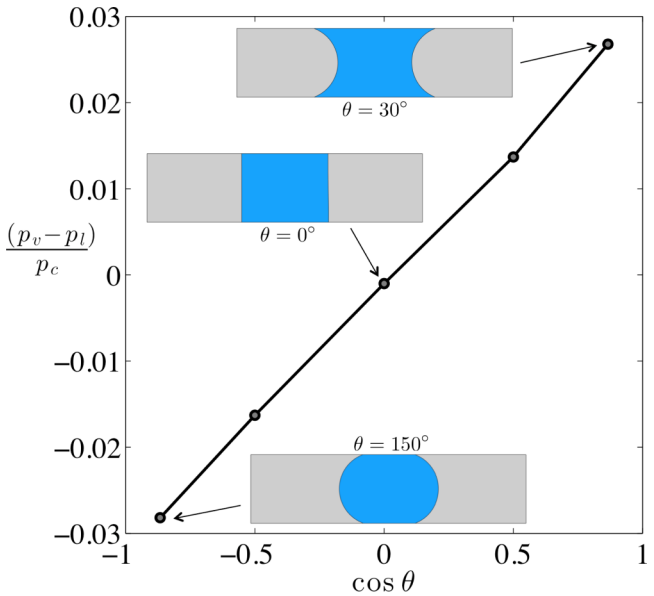

FIG. 4. Model validation using the Young-Laplace equation for a liquid slug. Using the same simulation setup as in Fig. 3, we measure the pressures inside the liquid and vapor phases, at points sufficiently far from the interface, and plot the pressure difference between the vapor and liquid phases, the capillary pressure $\Delta p_r = p_{rv} - p_{rl}$, against $\cos\theta$. The linear dependence between capillary pressure and $\cos\theta$ indicates that the model honors the Young-Laplace equation.

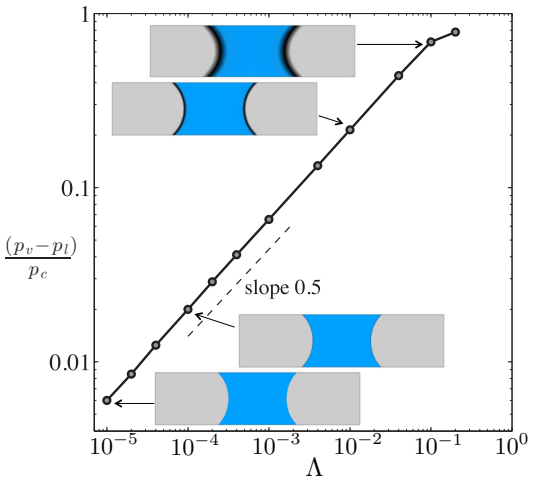

FIG. 5. The interface thickness, in a diffuse-interface model driven by a cubic equation of state δ, is controlled by the Korteweg number Λ. We compute the equilibrium density field for a liquid bridge in a microchannel with $\theta = 30^\circ$ and different values of Λ. We plot the capillary pressure against Λ and observe that our numerical simulations recover the theoretical scaling $\delta \sim \sqrt{\Lambda}$. In practice, this strong dependence of surface tension on interface thickness limits the use of these direct simulations to the micrometer scale, as the numerical discretization needs to be fine enough to capture the interface thickness that is consistent with the correct surface tension.

diffuse-interface models to the micrometer scale. As pointed out in [59], the effective dimensionless surface tension predicted by the diffuse-interface model σ_D scales like $\sigma_D \sim \sqrt{\Lambda}$. Since the interface width δ also scales with Λ, $\delta \sim \sqrt{\Lambda}$, it turns out that millimeter-scale simulations would require extremely fine grid resolutions to capture the interface thickness that is consistent with the physical surface tension of the system being studied. One potential solution to the artificial increase of surface tension is to modify the equation of state around the spinodal region [59]. While we are exploring this approach, the present study does not introduce any modifications on the EOS and therefore our simulations should be interpreted to be quantitatively accurate at the micrometer scale.

The implications of the scaling of interface thickness with the square root of Λ are of both theoretical and practical relevance. At a theoretical level, the sharp interface limit of the Navier-Stokes-Korteweg system has been analyzed using matched asymptotic expansions in the interface thickness [60,90]. From a physical perspective, Λ should be chosen to match the actual vapor-liquid surface tension at a given temperature. The practical problem with this latter choice is that resolving the corresponding interface thickness may be out of reach computationally. In this study we adopt a pragmatic approach: Given the grid resolution that we can afford for a given domain, we choose the smallest Λ that can be resolved with our grid, that is, $\Lambda \sim \delta x^2$, where δx is the typical mesh size.

To test the scaling between effective surface tension and Korteweg number Λ, we run simulations of steady-state liquid bridges with the same static contact angle $\theta = 45^\circ$ and different values of Λ. We let Λ vary over several orders of magnitude, which leads to liquid slugs that preserve their overall shape but have very different interface thicknesses. We observe that, as expected, the capillary pressure at equilibrium depends on Λ (Fig. 5) and our numerical simulations recover the theoretical scaling $\Delta p_r \sim \sqrt{\Lambda}$.

Finally, it is interesting to discuss the connection between interface thickness and surface tension in the present Korteweg model for immiscible flows [61,65], compared with the model of Korteweg stresses of apparent interfacial tension in miscible flows [91–94]. In the former, the width of the diffuse interface is set by a balance between the pressure behavior across the interface and the regularizing nature of the Korteweg stresses. Given the equation of state that governs the bulk fluid

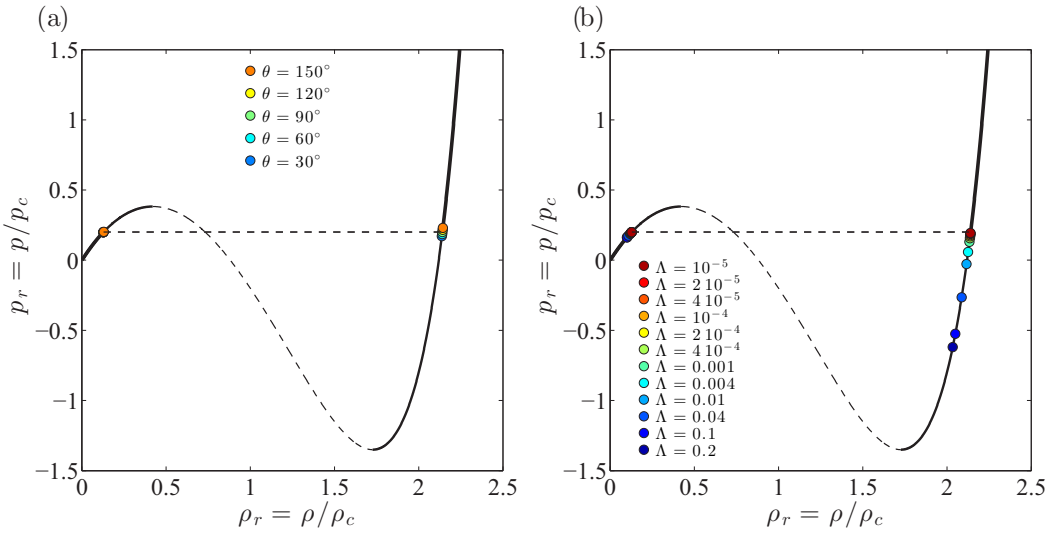

FIG. 6. Capillary pressure affects the equilibrium states of liquid and vapor densities. We study the liquid and vapor densities at equilibrium in the context of the liquid bridge simulations analyzed in Figs. 3–5. (a) For a relatively small Korteweg number $\Lambda = 10^{-4}$, the static contact angle only slightly alters the equilibrium densities, which remain close to the theoretical Maxwell states. (b) The increase in surface tension as Λ increases promotes much larger deviations from the equilibrium values and the liquid densities enter into the metastable region. The van der Waals pressure curve at this temperature $T_r = 0.7$ is plotted as a reference (black line).

behavior, surface tension increases as the strength of the Korteweg stresses increase (that is, as the interface thickness increases). In the miscible case, the width of the mixing region increases with time, which is the reason behind these stresses having a stabilizing effect on the miscible viscous fingering [95,96]. In this latter case, the effective surface tension is controlled by the concentration gradients: A thicker interface implies a smaller effective surface tension.

B. Impact of wetting conditions on phase densities

In the absence of curved interfaces, vapor and liquid pressures are equal at equilibrium. Capillary pressures, however, may alter the equilibrium states of liquid and vapor densities. In the context of the simulation of liquid bridges of the previous validation tests, we compare the liquid and vapor densities at equilibrium with the theoretical values (the Maxwell states) predicted by equilibrium considerations alone using the equation of state (Fig. 6). For a relatively small Korteweg number $\Lambda = 10^{-4}$, the static contact angle only slightly alters the equilibrium densities, which remain close to the theoretical Maxwell states [Fig. 6(a)]. As we increase Λ, however, the interface thickness and effective surface tension also increase, which induces stronger deviations from the theoretical vapor and liquid densities, suggesting that the steady-state values are metastable [Fig. 6(b)].

IV. MODEL VALIDATION: EVAPORATION FROM A CHANNEL

We perform further validation of our numerical model by simulating evaporation of a van der Waals fluid in a channel for different wetting conditions. This process is amenable, under certain simplifying assumptions that we detail below, to analytical modeling.

We consider a channel initially filled with a van der Waals fluid at a pressure p_0 for which the fluid is in liquid state, open at one end to pressure p_{out} for which the fluid is in gas state. This leads to an evaporation process in which the fluid evaporates and the meniscus recedes (with prescribed

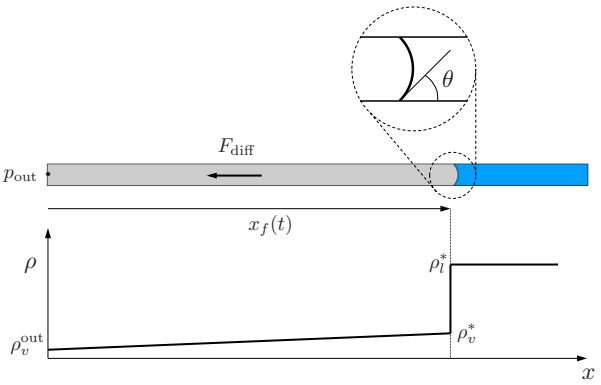

FIG. 7. Schematic of the validation problem simulating evaporation of a van der Waals fluid in a channel.

contact angle θ). We are interested in determining, as a function of time, the diffusive evaporative flux F_{diff} and the position of the evaporation front x_f (Fig. 7).

Equilibrium at the interface relates the fluid densities on the liquid and vapor sides ρ_l^* and ρ_v^*, respectively, which we assume remain constant throughout the evaporation process. These quantities are dependent on the interface curvature and therefore on the channel height H and the contact angle θ. To facilitate the development of a simple analytical model, we make two further assumptions: (i) The liquid density is uniform, such that $\rho_l = \rho_l^*$ and therefore independent of space and time, and (ii) the characteristic timescale for vapor diffusion $T_{\text{diff}} = L^2/D_v$ is much shorter than the characteristic timescale for meniscus advection $T_{\text{adv}} = L/\dot{x}_f$.

From mass conservation, $\dot{M} = -H\, F_{\text{diff}}^{\text{out}}$, where the mass of fluid in the channel is $M(t) = H\int_0^{x_f(t)} \rho_v(x;t)\,dx + H\int_{x_f(t)}^{L} \rho_l(x;t)\,dx$. From assumption (i) above and using the Leibnitz rule of integration, $\dot{M} = -H(\rho_l^* - \rho_v^*)\dot{x}_f$. From assumption (ii), the density profile is linear and the diffusive flux is uniform in the vapor phase, and given by Fick's law of diffusion $F_{\text{diff}} = -D_v d\rho_v/dx = -D_v(\rho_v^* - \rho_v^{\text{out}})/x_f$. Substituting these expressions for $\dot{M}$ and F_{diff} into the mass conservation equation, we arrive at the ordinary differential equation

$$\dot{x}_f = -D_v \frac{\rho_v^* - \rho_v^{\text{out}}}{\rho_l^* - \rho_v^*} \frac{1}{x_f}. \tag{39}$$

Solving this ordinary differential equation with the initial condition $x_f(t=0) = 0$, we obtain the equation for the evolution of the front position

$$x_f(t) = \left(2D_v \frac{\rho_v^* - \rho_v^{\text{out}}}{\rho_l^* - \rho_v^*}\right)^{1/2} t^{1/2}. \tag{40}$$

Substituting in the expression for the diffusive flux,

$$F_{\text{diff}}(t) = \left[\tfrac{1}{2} D_v\left(\rho_v^* - \rho_v^{\text{out}}\right)(\rho_l^* - \rho_v^*)\right]^{1/2} t^{-1/2}. \tag{41}$$

Equation (41) indicates a diffusive scaling of the evaporative flux ($F_{\text{diff}} \sim t^{-1/2}$) for all contact angles and suggests that the magnitude of the flux is controlled by the product $(\rho_v^* - \rho_v^{\text{out}})(\rho_l^* - \rho_v^*)$, which in turn depends on channel height H, surface tension σ, and contact angle θ.

In Fig. 8 we compare the two-dimensional simulation results with the analytical prediction multiplied by the channel height $H\,F_{\text{diff}}(t)$. We obtain the transition densities ρ_l^* and ρ_g^* from density profiles along the channel axis, obtained from the numerical simulations [Fig. 8(a)]. For the different contact angles, we obtain $\rho_v^* = 0.145$ and $\rho_l^* = 2.171$ (for $\theta = 135^\circ$), $\rho_v^* = 0.128$ and $\rho_l^* = 2.142$ (for $\theta = 90^\circ$), and $\rho_v^* = 0.114$ and $\rho_l^* = 2.11$ (for $\theta = 45^\circ$).

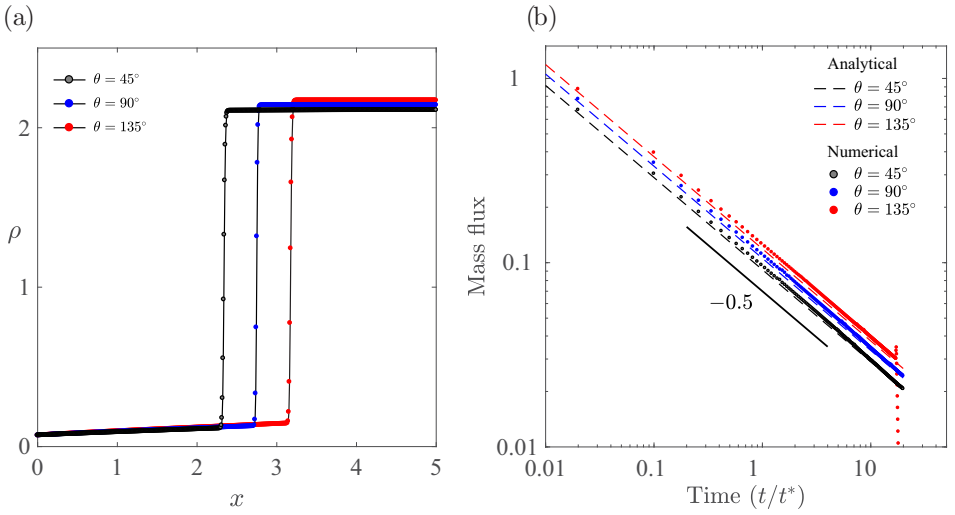

FIG. 8. Evaporation in a channel. The channel height is $H = 0.1$ units, and a density $\rho_v^{\text{out}} = 0.07$ is imposed at the left boundary. The initial density is $\rho_0 = 2.2$. (a) Reduced density profiles at time $t/t^* = 10$ for three static contact angles $\theta = 45°$, $90°$, and $135°$. (b) Comparison between numerical and analytical vapor fluxes (41) through the left boundary.

The diffusivity D_v is estimated from the model equation, focusing on the range on vapor diffusions away from the interface, for which we neglect higher-order spatial derivatives, so the model (36) reduces to a diffusion equation

$$\frac{\partial \rho_r}{\partial t} + \nabla \cdot (-D_v \nabla \rho_r) = 0, \tag{42}$$

with

$$D_v = \frac{\rho_r^2}{\mu_r}\frac{\partial \nu_r}{\partial \rho_r} = \frac{\rho_r^2}{\mu_r}\left[-6 + \frac{8T_r}{3(3-\rho_r)}\left(\frac{3}{\rho_r} - \frac{3}{3-\rho_r}\right)\right]. \tag{43}$$

We assume that the diffusivity is constant and we evaluate them at the transition vapor densities ρ_v^*. For $T_r = 0.7$ and the different contact angles, we arrive at $D_v = 18.62$ (for $\theta = 135°$), $D_v = 19.09$ (for $\theta = 90°$), and $D_v = 19.11$ (for $\theta = 45°$). The analytical solution (41) describes the evolution of mass fluxes observed in the numerical simulations accurately [Fig. 8(b)].

V. SPINODAL DECOMPOSITION OF A VAN DER WAALS FLUID IN A POROUS MEDIUM

As shown in the preceding section, wetting conditions and pore space structure may alter the equilibrium states of vapor-liquid systems in porous media. We further explore this phenomenon by studying the impact of wetting conditions and pore space geometry on phase ordering dynamics. A supercritical homogeneous fluid that is rapidly quenched below the critical temperature into the unstable region will undergo spinodal decomposition. After the initial separation phase, the pore domains occupied by the different phases will grow in a coarsening process that evolves towards the minimization of interfacial energy. In the bulk, the scaling regimes that ensue at long times are relatively well understood [21]. While it has been shown that hydrodynamic instabilities may arrest the coarsening process [76], the role of wetting conditions on liquid-vapor transitions in porous media remains largely unexplored. The practical relevance of these phase ordering processes lies in the fact that they may control the initial distribution of fluids within the pore space as well as phase

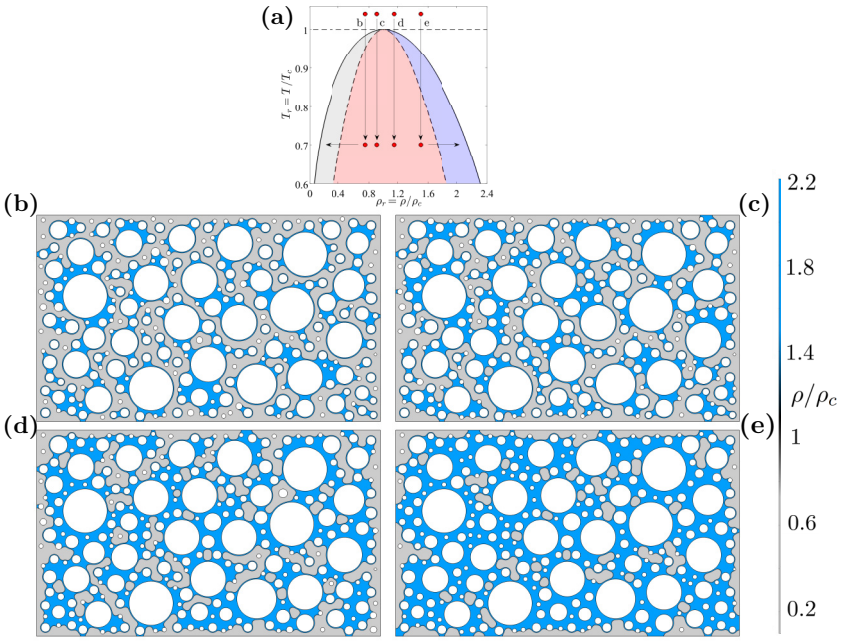

FIG. 9. Phase separation of a van der Waals fluid in porous media: density maps at dimensionless time $t_D = 50$, showing the arrest of coarsening due to the pore geometry and wetting conditions. We show results for the strongly wetting case $\theta = 0^\circ$ and mean densities (a) $\bar{\rho} = 0.750\,95$, (b) $\bar{\rho} = 0.901\,52$, (c) $\bar{\rho} = 1.1525$, and (d) $\bar{\rho} = 1.5038$. The temperature is $T_r = 0.7$ and the Korteweg number is $\Lambda = 2 \times 10^{-4}$. The initial density fields are random perturbations around the mean density.

connectivity. Phase connectivity is directly linked to phase mobility [97], while fluid-fluid interfacial areas control mass and heat transfer and equilibrium capillary pressures [98].

We simulate spinodal decomposition in porous media for various initial conditions (Figs. 9–11). In particular, the initial density fields are random perturbations around mean densities that are chosen to lie inside the spinodal region [Fig. 9(a)]. The synthetic porous medium is a micromodel of size 5×3 in dimensionless units, with circular obstacles of various diameters, and we enforce that the system is closed by imposing zero-flux boundary conditions. We focus on liquid-wet conditions, $\theta = 0^\circ$, and set the Korteweg number to $\Lambda = 2 \times 10^{-4}$. At time $t = 0$ the fluid is instantaneously quenched to a temperature $T_r = 0.7$, at which the homogeneous state is mechanically unstable. The equilibrium phase diagram for a van der Waals fluid [Fig. 9(a)] predicts that the initially single-phase system will segregate into domains of liquid and vapor, with densities corresponding to the Maxwell states (along the binodal line). We plot the density maps at dimensionless time $t_D = 50$, showing the arrest of coarsening due to the geometry and wetting conditions [Figs. 9(b)–9(e)]. We show results for mean densities $\bar{\rho} = 0.750\,95$ [Fig. 9(b)], $\bar{\rho} = 0.901\,52$ [Fig. 9(c)], $\bar{\rho} = 1.1525$ [Fig. 9(d)], and $\bar{\rho} = 1.5038$ [Fig. 9(e)]. The equilibrium phase densities, pressures, and fluid configurations are strongly affected by wetting conditions and pore space geometry (Fig. 10). The pressure maps at dimensionless time $t_D = 50$ illustrate a dependence of capillary pressure on fluid configurations. At least within the range of mean densities studied here, the capillary pressures at $t_D = 50$ depend only slightly on the final liquid-vapor volume fractions (Fig. 11).

VI. VAPORIZATION AND CONDENSATION FRONTS

We now turn to phase transitions driven by vaporizing and condensing fronts (Figs. 12–18). Assume a closed porous domain that is initially at equilibrium, saturated with liquid of density

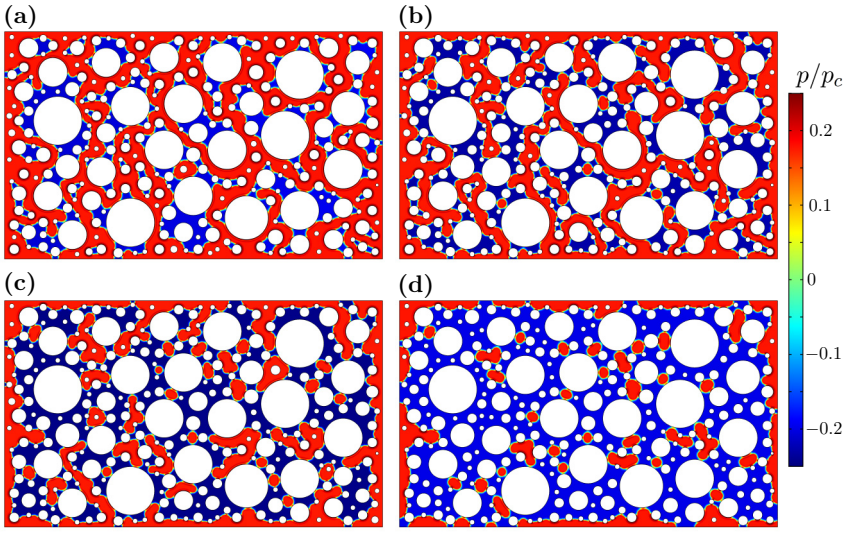

FIG. 10. Phase separation of a van der Waals fluid in porous media: pressure maps at dimensionless time $t_D = 50$, showing the arrest of coarsening due to the geometry and wetting conditions. We show results for the strongly wetting case $\theta = 0^\circ$ and mean densities (a) $\bar{\rho} = 0.750\,95$, (b) $\bar{\rho} = 0.901\,52$, (c) $\bar{\rho} = 1.1525$, and (d) $\bar{\rho} = 1.5038$. The temperature is $T_r = 0.7$ and the Korteweg number is $\Lambda = 2 \times 10^{-4}$. Note that the final liquid pressures (and therefore densities) vary with the final liquid volume fraction.

$\rho_{r0} = 2.2$, at temperature $T_r = 0.7$. We force phase transition by decreasing the pressure at the left boundary while the other boundaries remain no-flow walls, which induces a net mass flow out of the domain. We impose a density $\rho_{rLB} = 0.07$ at the left boundary, which triggers a vaporizing front where liquid vaporizes at the liquid-vapor interface and flows out of the domain. The structure of the

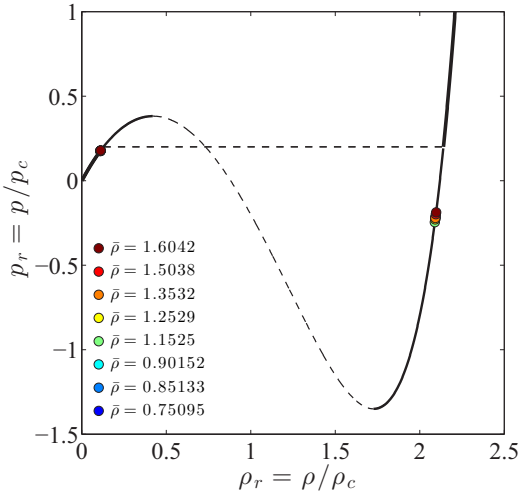

FIG. 11. Phase separation of a van der Waals fluid in porous media: metastable density states after long-time simulations of phase separation. We plot the equilibrium densities in the van der Waals pressure-density curves. The simulations correspond to those of Figs. 9 and 10 plus other additional cases not shown above. Note that the key driver behind the nonequilibrium densities is the capillary pressure, controlled by surface tension and pore size distribution rather than the mean density or initial conditions.

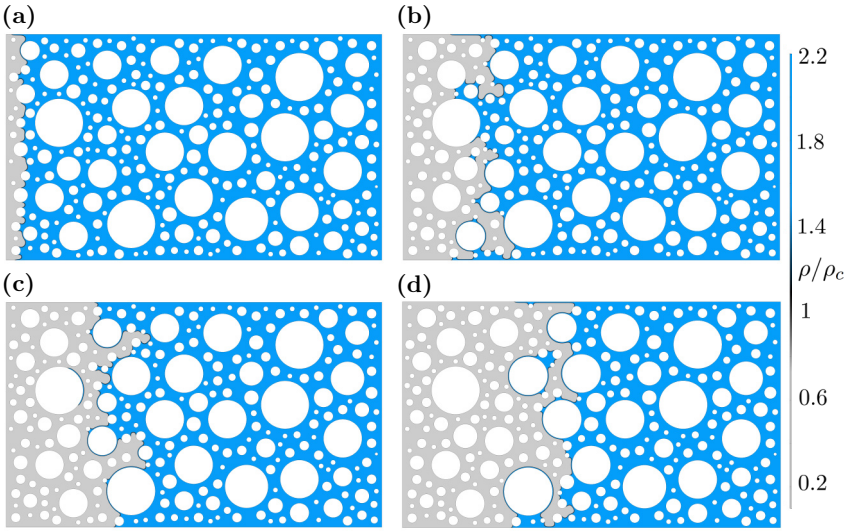

FIG. 12. Simulation of a vaporizing front in a micromodel. The internal domain walls are strongly wetting to the liquid phase ($\theta = 0^\circ$). A closed porous domain is initially filled with liquid of density $\rho_{r0} = 2.2$ at temperature $T_r = 0.7$. We force phase transition by decreasing the pressure at the left boundary, while the others remain no-flow walls. The low boundary pressure, enforced by imposing a density $\rho_{rLB} = 0.07$, triggers a phase change front where liquid vaporizes at the liquid-vapor interface and flows out of the domain.

displacement front and individual interface displacements depend on the wetting conditions. Here we show sample cases in which the vapor phase may be the nonwetting phase ($\theta = 0^\circ$, Fig. 12) or the wetting phase ($\theta = 180^\circ$, Fig. 13). The overall dynamics of the vaporizing fronts are consistent with

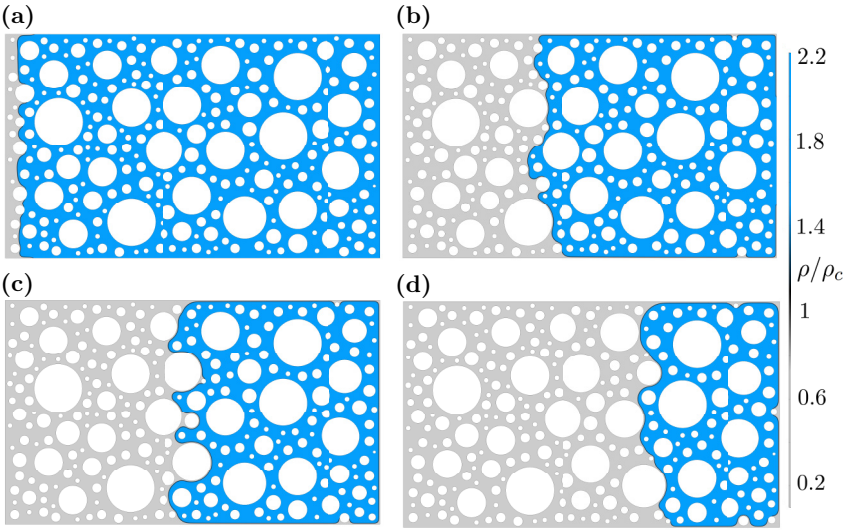

FIG. 13. Simulation of a vaporizing front in a micromodel. The internal domain walls are strongly wetting to the vapor phase ($\theta = 180^\circ$). A closed porous domain is initially filled with liquid of density $\rho_{r0} = 2.2$ at temperature $T_r = 0.7$. We force phase transition by decreasing the pressure at the left boundary, while the others remain no-flow walls. The low boundary pressure, enforced by imposing a density $\rho_{rLB} = 0.07$, triggers a phase change front where liquid vaporizes at the liquid-vapor interface and flows out of the domain.

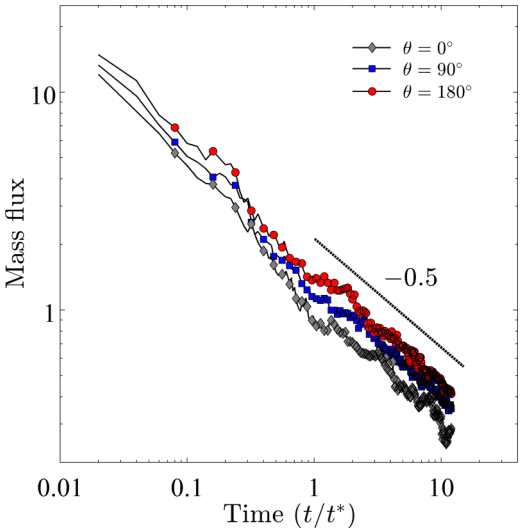

FIG. 14. Time evolution of mass fluxes for different static contact angles during the advance of a vaporizing front in a micromodel (including the simulations in Figs. 12 and 13). These results indicate that the simulated phase change fronts can be understood as simple diffusion-limited processes.

a diffusion-limited process, in particular mass fluxes that decay with the square root of time (Fig. 14). The diffusion-limited nature of the process can be rationalized by considering that liquid vaporizes along the front and then flows out of the domain following a Darcy-type flow. The drainage case $\theta = 0^\circ$ is conceptually similar to the classical drying problem, as is controlled by heterogeneity in the pore geometry. To illustrate the impact of heterogeneity in the front advance patterns, we repeat the simulation of vaporizing front in the liquid-wet conditions with a distribution of obstacles that

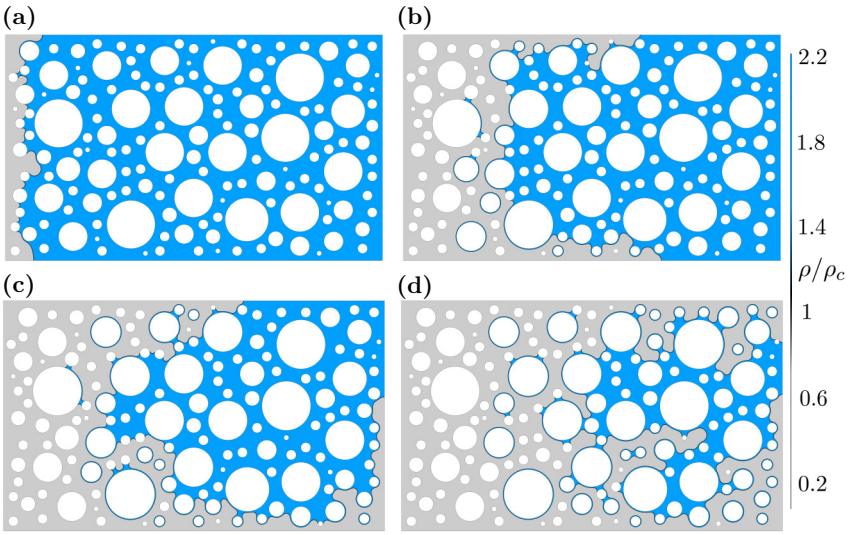

FIG. 15. Vaporizing front patterns are controlled by heterogeneity of the pore space. We show snapshots of a simulation with the same conditions as those of Fig. 13 ($\rho_{r0} = 2.2$, $\rho_{rLB} = 0.07$, $T_r = 0.7$, and $\theta = 0^\circ$) but with a distribution of obstacles that slightly promotes imbibition along the top and bottom boundaries. These patterns of vapor invasion resemble the invasion-percolation-like fronts in capillary fingering, as proposed in the context of drying [83,84].

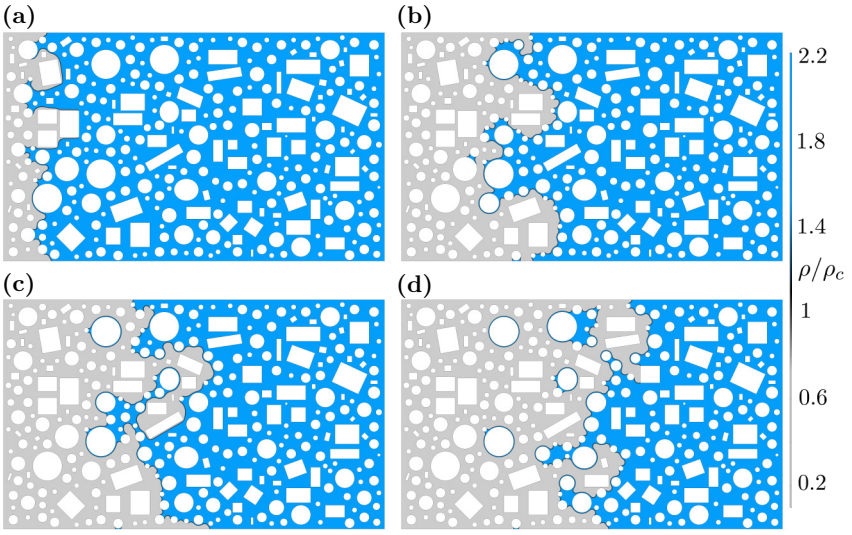

FIG. 16. Vaporizing front patterns under mixed-wet conditions. We show snapshots of a simulation with the same conditions as those of Fig. 13 ($\rho_{r0} = 2.2$, $\rho_{rLB} = 0.07$, and $T_r = 0.7$) but with a distribution of circular and rectangular obstacles. In this case the quadrilateral obstacles are strongly wetting to the vapor phase $\theta = 180°$, while the circular ones are strongly wetting to the liquid phase $\theta = 0°$. See also video 1 in the Supplemental Material [99].

slightly promotes imbibition along the top and bottom boundaries (Fig. 15). The resulting patterns of vapor invasion resemble the invasion-percolationlike fronts in capillary fingering, as proposed in the context of drying [83,84].

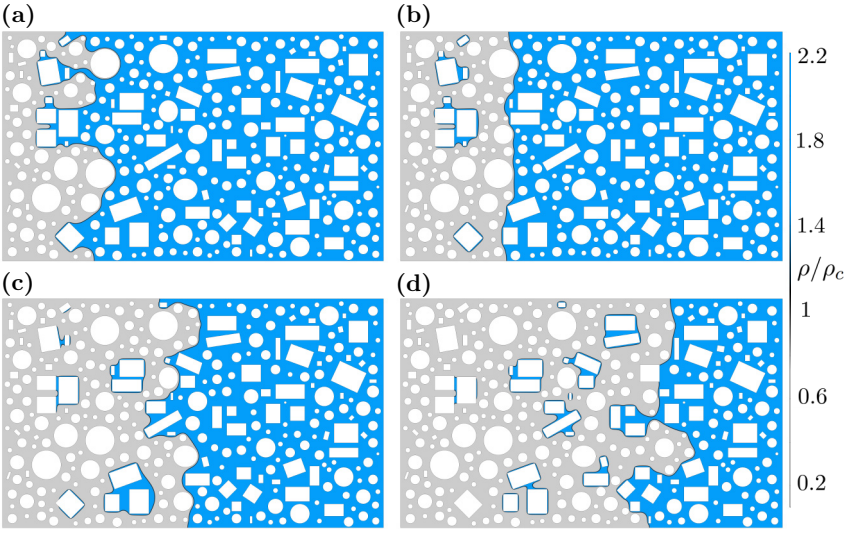

FIG. 17. Vaporizing front patterns under mixed-wet conditions. We show snapshots of a simulation with the same conditions as those of Fig. 13 ($\rho_{r0} = 2.2$, $\rho_{rLB} = 0.07$, and $T_r = 0.7$) but with a distribution of circular and rectangular obstacles. In this case the quadrilateral obstacles are strongly wetting to the liquid phase $\theta = 0°$, while the circular ones are strongly wetting to the vapor phase $\theta = 180°$. See also video 2 in the Supplemental Material [99].

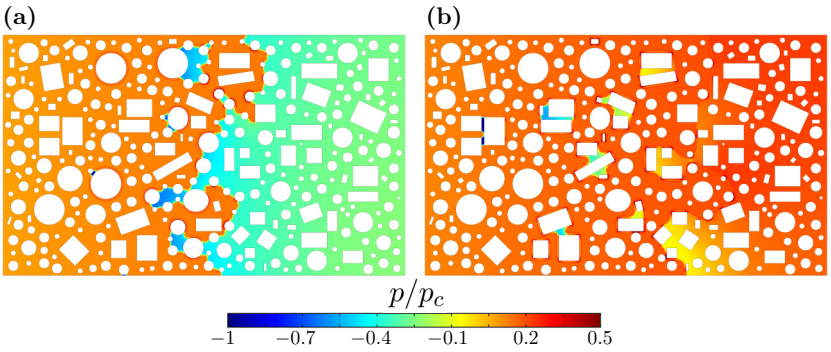

FIG. 18. Pressure maps at the end of the simulations (dimensionless time $t_D = 12$) for the two mixed-wetting cases shown in Figs. 16 and 17. The pockets of residual liquid remain at metastable conditions at very low pressures.

Finally, we consider vaporizing front patterns under mixed-wet conditions (Figs. 16–19). We generate micromodel geometries composed of circular and quadrilateral obstacles. In one case the quadrilateral obstacles are strongly wetting to the vapor phase $\theta = 180°$, while the circular ones are strongly wetting to the liquid phase $\theta = 0°$ (Fig. 16; see also video 1 in the Supplemental Material [99]). Alternatively, we also consider the case where the quadrilateral obstacles are strongly wetting to the liquid phase $\theta = 0°$(Fig. 17; see also video 2 in the Supplemental Material [99]). The rougher geometry of the quadrilateral obstacles tends to induce more persistent residual pockets of metastable liquid at very low pressures (Fig. 18). The time evolution of mass fluxes for the two mixed-wetting cases indicates that vapor fluxes depend slightly on the grain roughness and wetting conditions (Fig. 19).

VII. PRESSURE FLUCTUATIONS AND PRESSURE PULSES DUE TO ADVANCING INTERFACES

One of the main objectives of direct simulation or multiphase displacements in porous media is to provide insights into the potential role of pore-scale fluctuations on representative-elementary-

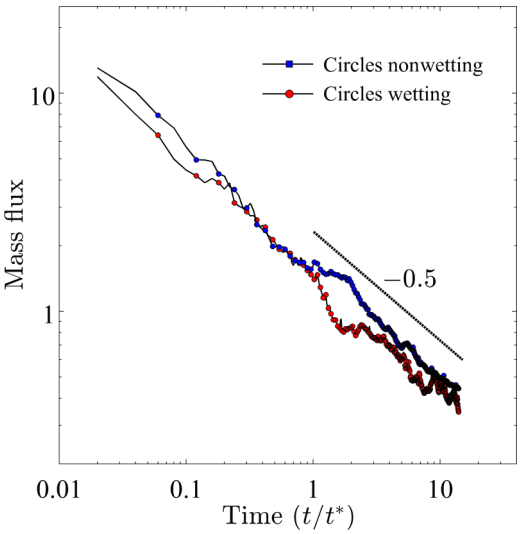

FIG. 19. Time evolution of mass fluxes for the two mixed-wetting cases shown in Figs. 16 and 17 during the advance of a vaporizing front in a micromodel. These results indicate that the simulated phase change fronts can be understood as simple diffusion-limited processes.

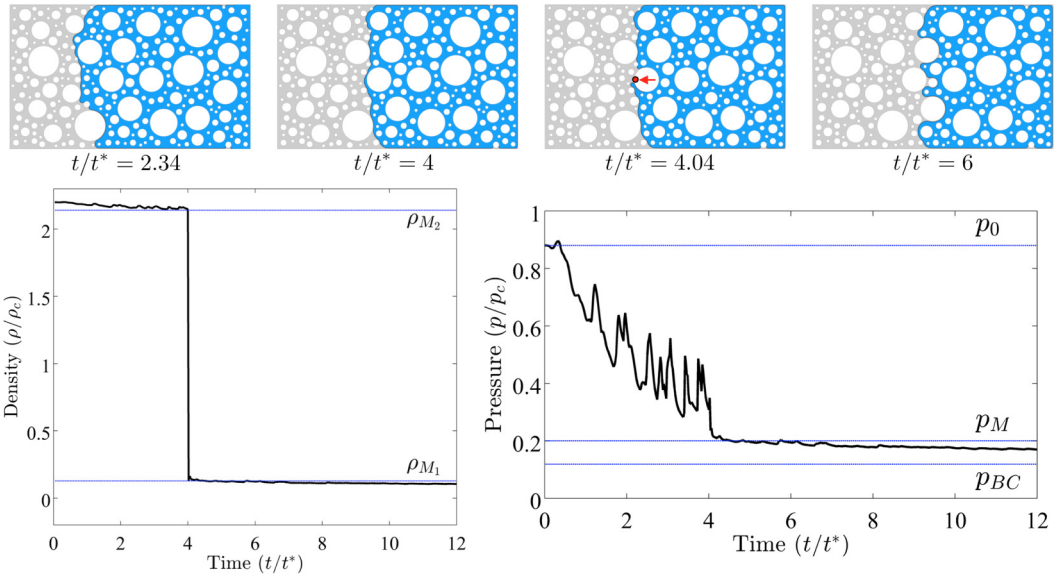

FIG. 20. Pressure and density fluctuations associated with the advancement of interfaces and the rupture of liquid films. We show the time evolution of density and pressure at a location at the surface of an obstacle (indicated with a red dot), together with snapshots of the density field immediately before and after the front has reached this location. The model parameters are $\rho_{r0} = 2.2$, $\rho_{rLB} = 0.07$, $T_r = 0.7$, and $\theta = 180^\circ$. The Maxwell densities ρ_{M_1} and ρ_{M_2}, which are the thermodynamic equilibrium densities of vapor and liquid at this temperature, are indicated with dashed blue lines. The initial, left-boundary, and Maxwell pressures p_0, p_{BC}, and p_M, respectively, are also indicated with dashed blue lines. The large pressure perturbations as the interface advances correspond to the propagation of pressure waves generated when interfaces move or break. In this imbibition case, the transition densities correspond almost exactly to those of theoretical equilibrium (indicated with dashed blue lines). The pressure is higher than the theoretical pressure on the liquid side of the interface p_M due to surface tension.

volume quantities. In this section we show that the proposed diffuse-interface model is able to capture pressure fluctuations generated as liquid-vapor interfaces advance, in accordance with experimental observations [77–82] (Figs. 20–23).

The pressure signatures inside the liquid phase depend strongly on the wetting conditions. To illustrate this dependence, we track the evolution of pressure at a point inside the domain and concentrate on the pressure fluctuations as the vaporizing front reaches the point and moves past it. In the imbibition case, when the vapor phase is the wetting phase ($\theta = 180^\circ$), the transition densities correspond almost exactly to those of theoretical equilibrium (Fig. 20). The pressure is higher than the theoretical one on the liquid side of the interface due to surface tension, and pressure fluctuates as a result of the advance of interfaces and film breakup as the vaporizing front advances. In the neutrally wetting case ($\theta = 90^\circ$, Fig. 21), the pressures oscillate around the theoretical transition pressure, without major differences between the liquid and vapor pressures (zero capillary pressure). Finally, the drainage case exhibits large pressure fluctuations, and pressures inside the vapor phase are significantly higher than in the liquid phase ($\theta = 0^\circ$, Fig. 22), which is consistent with a large capillary pressure. As expected, pressure fluctuations associated with the advancement of interfaces and film breakup are much larger in the liquid phase, which is less compressible (Fig. 23).

Pressure perturbations induced by interfacial processes propagate as pulses inside the low-compressibility liquid phase (Fig. 24). The structure of acoustic emissions during two-phase displacements has been proposed as a proxy to understand the flow processes involved [77]. Our model can simulate the propagation of these pressure pulses and the interaction of pressure

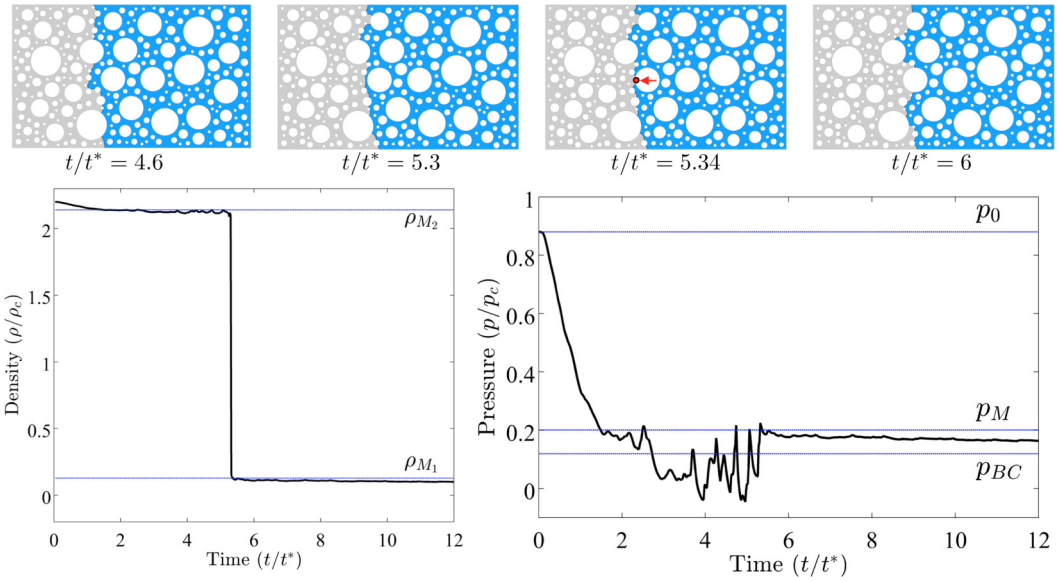

FIG. 21. Pressure and density fluctuations associated with the advancement of interfaces and the rupture of liquid films. We show the time evolution of density and pressure at a location at the surface of an obstacle (indicated with a red dot), together with snapshots of the density field immediately before and after the front has reached this location. The model parameters are $\rho_{r0} = 2.2$, $\rho_{rLB} = 0.07$, $T_r = 0.7$, and $\theta = 90^\circ$. The Maxwell densities ρ_{M_1} and ρ_{M_2}, which are the thermodynamic equilibrium densities of vapor and liquid at this temperature, are indicated with dashed blue lines. The initial, left-boundary, and Maxwell pressures p_0, p_{BC}, and p_M, respectively, are also indicated with dashed blue lines. In this neutrally wetting case, pressures oscillate around the theoretical transition pressure p_M without major differences between the liquid and vapor pressures (zero capillary pressure).

fluctuations with other flow mechanisms. In Fig. 24 we show a sequence of density and pressure maps at different time levels, illustrating the evolution of a pressure pulse generated by the breakup of a liquid film at the evaporation front in the drainage case ($\theta = 0^\circ$).

VIII. CONCLUSION

In this study we developed a diffuse-interface model for the simulation of liquid-vapor flow of a van der Waals fluid at the pore scale. In our model, we simplified the Navier-Stokes hydrodynamics by proposing a Darcy-Korteweg model to describe liquid-vapor flows in Hele-Shaw cells or micromodels.

We validated our model by comparing the vapor and liquid pressures with the theoretical values from the Young-Laplace equation for a liquid bridge in a narrow channel and for various static contact angles. We further showed that the model satisfies the theoretical scaling between the interface thickness (through the Korteweg number Λ) and the effective surface tension. The strong dependence of surface tension on the interface width, which is a numerical parameter, emerges as one of the major challenges in the simulation of fluid mixtures described by equations of state at the pore scale.

We applied the model to study the impact of wetting conditions and pore space geometry on phase ordering dynamics during phase segregation and showed that capillarity has two notable effects on spinodal decomposition: (i) Capillarity alters the steady-state vapor and liquid states, leading to metastable phases, and (ii) wetting conditions and the structure of the pore space may arrest the coarsening process, controlling the distribution of fluid phases in the pore space. These results are important, because phase connectivity is directly linked to phase mobility, while fluid-fluid interfacial areas control mass and heat transfer and equilibrium capillary pressures.

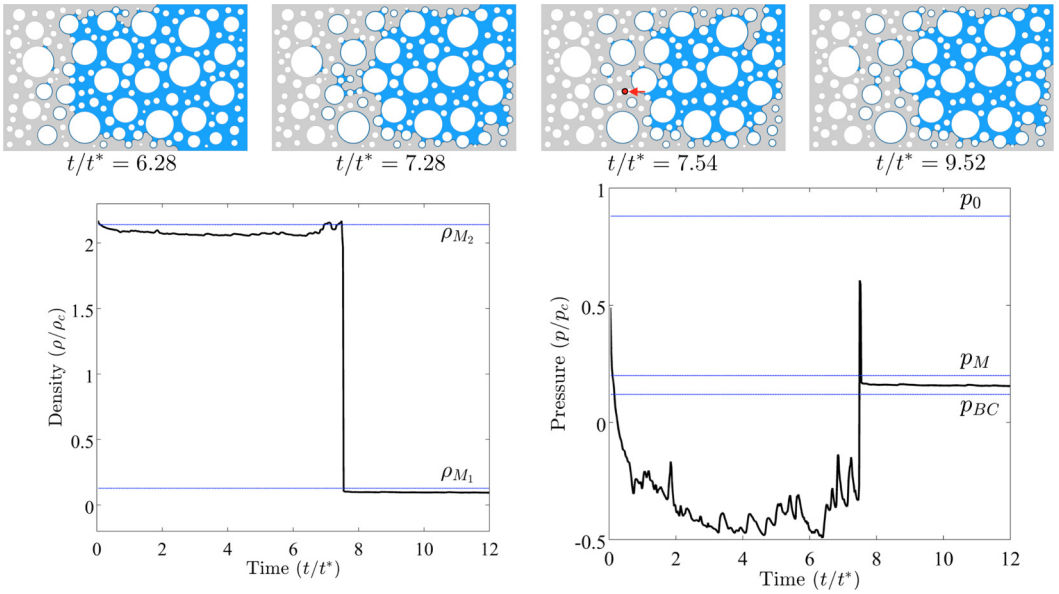

FIG. 22. Pressure and density fluctuations associated with the advancement of interfaces and the rupture of liquid films. We show the time evolution of density and pressure at a location at the surface of an obstacle (indicated with a red dot), together with snapshots of the density field immediately before and after the front has reached this location. The model parameters are $\rho_{r0} = 2.2$, $\rho_{rLB} = 0.07$, $T_r = 0.7$, and $\theta = 0^\circ$. The Maxwell densities ρ_{M_1} and ρ_{M_2}, which are the thermodynamic equilibrium densities of vapor and liquid at this temperature, are indicated with dashed blue lines. The initial, left-boundary, and Maxwell pressures p_0, p_{BC}, and p_M, respectively, are also indicated with dashed blue lines. In this case of drainage, pressures inside the vapor phase are significantly higher than in the liquid phase, which is consistent with a large capillary pressure.

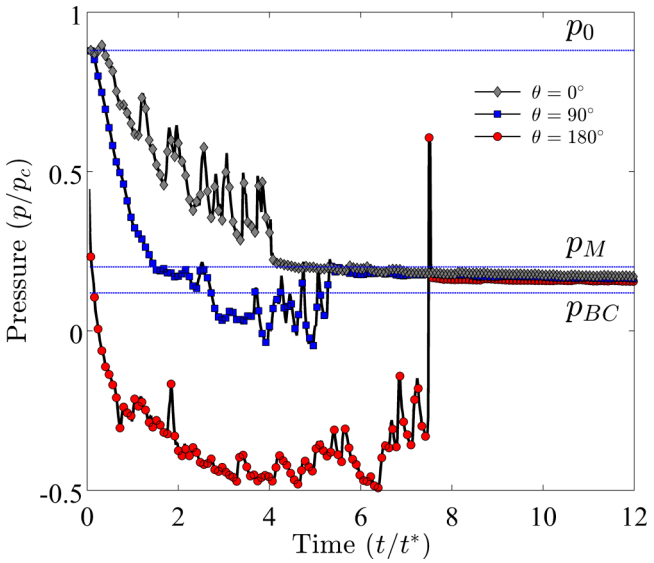

FIG. 23. Pressure and density fluctuations associated with the advancement of interfaces and the rupture of liquid films. A summary of the time evolution results shows the differences in pressure behavior with the wetting properties of the system.

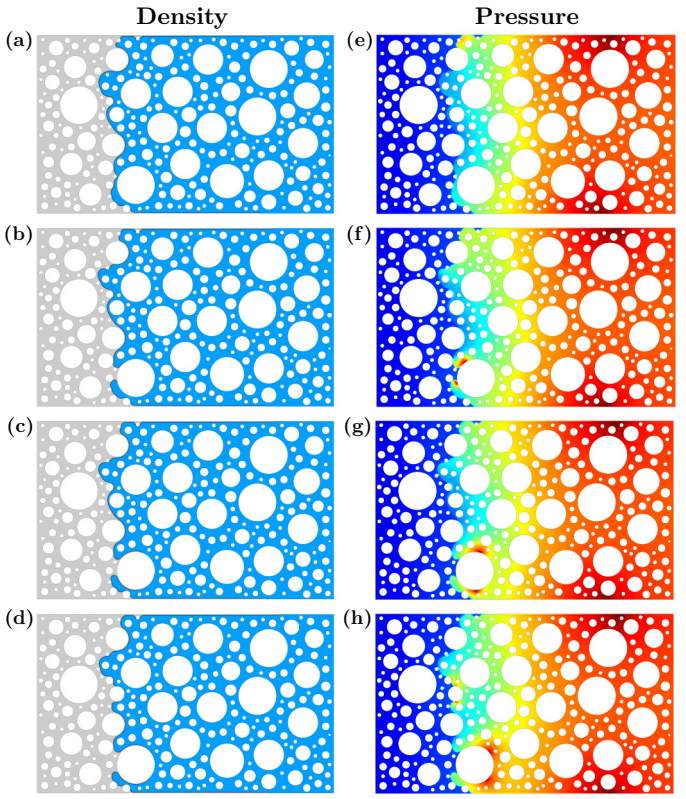

FIG. 24. Propagation of pressure fluctuations generated by the advance of the vaporizing front. We show (a)–(d) density maps at different time levels and (e)–(h) the corresponding pressure maps, illustrating the propagation of a pressure pulse generated by the breakup of a liquid film at the front.

Finally, we studied the dynamics of vaporization and condensation fronts under different wetting scenarios, including mixed-wet conditions. In particular, we showed that the diffuse-interface model is able to capture pressure fluctuations generated as liquid-vapor interfaces advance, in accordance with experimental observations.

While the gap-averaged two-dimensional approach has been very successful and insightful in describing important nonlinear features of the hydrodynamics of multiphase flows [41,43,100–106], it has some limitations. In particular, it cannot resolve the formation of fluid wedges at corners for strongly wetting systems [107–112], which exert an important control on the hydraulic continuity of the liquid phase [113,114] and therefore on evaporation rates [115]. Our model can be extended to three dimensions, where the hydrodynamics in the bulk fluid are described by the Navier-Stokes equations. This three-dimensional description will allow us to compare the dynamics of interfacial jumps with direct observations at the pore scale [78,116–119] and evaporation rates in porous media at the macroscopic scale [120,121].

ACKNOWLEDGMENTS

L.C.-F. gratefully acknowledges funding from the Spanish Ministerio de Economía y Competitividad (Grants No. CTM2014-54312-P and No. RYC-2012-11704). L.C.-F. and R.J. gratefully acknowledge funding from the MIT International Science and Technology Initiatives, through a Seed Fund grant.

[1] M. J. Blunt, B. Bijeljic, H. Dong, O. Gharbi, S. Iglauer, P. Mostaghimi, A. Paluszny, and C. Pentland, Pore-scale imaging and modeling, Adv. Water Resour. **51**, 197 (2013).
[2] A. Q. Raeini, B. Bijeljic, and M. J. Blunt, Numerical modelling of sub-pore scale events in two-phase flow through porous media, Transp. Porous Med. **101**, 191 (2014).
[3] A. Q. Raeini, M. J. Blunt, and B. Bijeljic, Direct simulations of two-phase flow on micro-CT images of porous media and upscaling of pore-scale forces, Adv. Water Resour. **74**, 116 (2014).
[4] W. G. Gray, A. L. Dye, J. E. McClure, L. J. Pyrak-Nolte, and C. T. Miller, On the dynamics and kinematics of two-fluid-phase flow in porous media, Water Resour. Res. **51**, 5365 (2015).
[5] C. Pan, M. Hilpert, and C. T. Miller, Lattice-Boltzmann simulation of two-phase flow in porous media, Water Resour. Res. **40**, W01501 (2004).
[6] Q. Kang, P. C. Lichtner, and D. Zhang, Lattice Boltzmann pore-scale model for multicomponent reactive transport in porous media, J. Geophys. Res. **111**, B05203 (2006).
[7] M. G. Schaap, M. L. Porter, B. S. B. Christensen, and D. Wildenschild, Comparison of pressure-saturation characteristics derived from computed tomography and Lattice Boltzmann simulations, Water Resour. Res. **43**, W12S06 (2007).
[8] M. L. Porter, M. G. Schaap, and D. Wildenschild, Lattice-Boltzmann simulations of the capillary pressure-saturation-interfacial area relationship for porous media, Adv. Water Resour. **32**, 1632 (2009).
[9] H. Liu, A. J. Valocchi, Q. Kang, and C. Werth, Pore-scale simulations of gas displacing liquid in a homogeneous pore network using the lattice Boltzmann method, Transp. Porous Med. **99**, 555 (2013).
[10] H. Liu, A. J. Valocchi, C. Werth, Q. Kang, and M. Oostrom, Pore-scale simulation of liquid CO_2 displacement of water using a two-phase lattice Boltzmann model, Adv. Water Resour. **73**, 144 (2014).
[11] M. Renardy, Y. Renardy, and J. Li, Numerical simulation of moving contact line problems using a volume-of-fluid method, J. Comput. Phys. **171**, 243 (2001).
[12] A. Q. Raeini, M. J. Blunt, and B. Bijeljic, Modelling two-phase flow in porous media at the pore scale using the volume-of-fluid method, J. Comput. Phys. **231**, 5653 (2012).
[13] A. Ferrari and I. Lunati, Direct numerical simulations of interface dynamics to link capillary pressure and total surface energy, Adv. Water Resour. **57**, 19 (2013).
[14] A. Ferrari and I. Lunati, Inertial effects during irreversible meniscus reconfiguration in angular pores, Adv. Water Resour. **74**, 1 (2014).
[15] A. Ferrari, J. Jimenez-Martinez, T. Le Borgne, Y. Méheust, and I. Lunati, Challenges in modeling unstable two-phase flow experiments in porous micromodels, Water Resour. Res. **51**, 1381 (2015).
[16] S. Osher and J. A. Sethian, Fronts propagating with curvature-dependent speed: Algorithms based on Hamilton-Jacobi formulations, J. Comput. Phys. **79**, 12 (1981).
[17] M. Prodanović and S. L. Bryant, A level set method for determining critical curvatures for drainage and imbibition, J. Colloid. Interface Sci. **304**, 442 (2006).
[18] E. Jettestuen, J. O. Helland, and M. Prodanović, A level set method for simulating capillary-controlled displacements at the pore scale with nonzero contact angles, Water Resour. Res. **49**, 4645 (2013).
[19] J. W. Cahn and J. E. Hilliard, Free energy of a nonuniform system. I. Interfacial free energy, J. Chem. Phys. **28**, 258 (1958).
[20] J. W. Cahn, On spinodal decomposition, Acta Metall. **9**, 795 (1961).
[21] A. J. Bray, Theory of phase-ordering kinetics, Adv. Phys. **43**, 357 (1994).
[22] D. M. Anderson, G. B. McFadden, and A. A. Wheeler, Diffuse-interface methods in fluid mechanics, Annu. Rev. Fluid Mech. **30**, 139 (1998).
[23] L. K. Antanovskii, A phase-field model of capillarity, Phys. Fluids **7**, 747 (1995).
[24] D. Jasnow and J. Viñals, Coarse-grained description of thermo-capillary flow, Phys. Fluids **8**, 660 (1996).
[25] J. S. Lowengrub and L. Truskinovsky, Quasi-incompressible Cahn-Hilliard fluids and topological transitions, Proc. R. Soc. A **454**, 2617 (1998).
[26] D. Jacqmin, Calculation of two-phase Navier-Stokes flows using phase-field modeling, J. Comput. Phys. **155**, 96 (1999).
[27] D. Jacqmin, Contact-line dynamics of a diffuse fluid interface, J. Fluid Mech. **402**, 57 (2000).
[28] F. Boyer, A theoretical and numerical model for the study of incompressible mixture flows, Comput. Fluids **31**, 41 (2002).

[29] V. E. Badalassi, H. D. Ceniceros, and S. Banerjee, Computation of multiphase systems with phase field models, J. Comput. Phys. **190**, 371 (2003).
[30] P. Yue, J. J. Feng, C. Liu, and J. Shen, A diffuse-interface method for simulating two-phase flows of complex fluids, J. Fluid Mech. **515**, 293 (2004).
[31] J. Kim, A continuous surface tension force formulation for diffuse-interface models, J. Comput. Phys. **204**, 784 (2005).
[32] H. Ding, P. D. M. Spelt, and C. Shu, Diffuse interface model for incompressible two-phase flows with large density ratios, J. Comput. Phys. **226**, 2078 (2007).
[33] A. G. Lamorgese and R. Mauri, Diffuse-interface modeling of phase segregation in liquid mixtures, Int. J. Multiph. Flow **34**, 987 (2008).
[34] J. Kim, A generalized continuous surface tension force formulation for phase-field models for multi-component immiscible fluid flows, Comput. Methods Appl. Mech. Eng. **198**, 3105 (2009).
[35] Y. Sun and C. Beckermann, Diffuse interface modeling of two-phase flows based on averaging: Mass and momentum equations, Physica D **198**, 281 (2004).
[36] M. E. Gurtin, Generalized Ginzburg-Landau and Cahn-Hilliard equations based on a microforce balance, Physica D **92**, 178 (1994).
[37] H. A. Akhlaghi Amiri and A. A. Hamouda, Evaluation of level set and phase field methods in modeling two phase flow with viscosity contrast through dual-permeability porous medium, Int. J. Multiph. Flow **52**, 22 (2013).
[38] F. O. Alpak, B. Riviere, and F. Frank, A phase-field method for the direct simulation of two-phase flows in pore-scale media using a non-equilibrium wetting boundary condition, Comput. Geosci. **20**, 881 (2016).
[39] H. A. Akhlaghi Amiri and A. A. Hamouda, Pore-scale modeling of non-isothermal two phase flow in 2D porous media: Influences of viscosity, capillarity, wettability and heterogeneity, Int. J. Multiph. Flow **61**, 14 (2014).
[40] L. Cueto-Felgueroso and R. Juanes, Nonlocal Interface Dynamics and Pattern Formation in Gravity-Driven Unsaturated Flow through Porous Media, Phys. Rev. Lett. **101**, 244504 (2008).
[41] L. Cueto-Felgueroso and R. Juanes, Macroscopic Phase-Field Model of Partial Wetting: Bubbles in a Capillary Tube, Phys. Rev. Lett. **108**, 144502 (2012).
[42] A. A. Pahlavan, L. Cueto-Felgueroso, G. H. McKinley, and R. Juanes, Thin Films in Partial Wetting: Internal Selection of Contact-Line Dynamics, Phys. Rev. Lett. **115**, 034502 (2015).
[43] L. Cueto-Felgueroso and R. Juanes, A phase-field model of two-phase Hele-Shaw flow, J. Fluid Mech. **758**, 522 (2014).
[44] K. H. Coats, An equation of state compositional model, Soc. Pet. Eng. J. **20**, 363 (1980).
[45] L. C. Young and R. E. Stephenson, A generalized compositional approach for reservoir simulation, Soc. Pet. Eng. J. **23**, 727 (1983).
[46] G. Acs, S. Doleschall, and E. Farkas, General purpose compositional model, Soc. Pet. Eng. J. **25**, 543 (1985).
[47] M. Michelsen and J. Mollerup, *Thermodynamic Models: Fundamentals & Computational Aspects* (Tie-Line, Copenhagen, 2007).
[48] D. V. Voskov and H. A. Tchelepi, Comparison of nonlinear formulations for two-phase multi-component EoS based simulation, J. Pet. Sci. Eng. **82–83**, 101 (2012).
[49] C. Appert and S. Zaleski, Lattice Gas with a Liquid-Gas Transition, Phys. Rev. Lett. **64**, 1 (1990).
[50] D. H. Rothman and S. Zaleski, Lattice-gas models of phase separation: interfaces, phase transitions, and multiphase flow, Rev. Mod. Phys. **66**, 1417 (1994).
[51] L. B. Di Pietro, A. Melayah, and S. Zaleski, Modeling water infiltration in unsaturated porous media by interacting lattice gas-cellular automata, Water Resour. Res. **30**, 2785 (1994).
[52] V. Pot, C. Appert, A. Melayah, D. H. Rothman, and S. Zaleski, Interacting lattice gas automaton study of liquid-gas properties in porous media, J. Phys. II France **6**, 1517 (1996).
[53] A. D. Angelopoulos, V. N. Paunov, Burganos, and A. C. Payatakes, Lattice Boltzmann simulation of nonideal vapor-liquid flow in porous media, Phys. Rev. E **57**, 3237 (1998).
[54] M. C. Sukop and D. Or, Invasion percolation of single component, multiphase fluids with lattice Boltzmann models, Physica B **338**, 298 (2003).

[55] M. C. Sukop and D. Or, Lattice Boltzmann method for modeling liquid-vapor interface configurations in porous media, Water Resour. Res. **40**, W01509 (2004).
[56] M. C. Sukop and D. Or, Lattice Boltzmann method for homogeneous and heterogeneous cavitation, Phys. Rev. E **71**, 046703 (2005).
[57] L. Di G. Sigalotti, J. Troconis, E. Sira, and F. Peña-Polo, Diffuse-interface modeling of liquid-vapor coexistence in equilibrium drops using smoothed particle hydrodynamics, Phys. Rev. E **90**, 013021 (2014).
[58] J. Serrin and J. E. Dunn, On the thermomechanics of interstitial working, Arch. Ration. Mech. Anal. **88**, 95 (1985).
[59] D. Jamet, O. Lebaigue, N. Coutris, and J. M. Delhaye, The second gradient method for the direct numerical simulation of liquid-vapor flows with phase change, J. Comput. Phys. **169**, 624 (2001).
[60] D. Diehl, J. Kremser, D. Kröner, and C. Rohde, Numerical solution of Navier-Stokes-Korteweg systems by local discontinuous Galerkin methods in multiple space dimensions, Appl. Math. Comput. **272**, 309 (2016).
[61] H. Gomez, T. J. R. Hughes, X. Nogueira, and V. M. Calo, Isogeometric analysis of the isothermal Navier-Stokes-Korteweg equations, Comput. Meth. Appl. Mech. Eng. **199**, 1828 (2010).
[62] A. Pecenko, L. G. M. van Deurzen, J. G. M. Kuerten, and C. W. M. van der Geld, Non-isothermal two-phase flow with a diffuse-interface model, Int. J. Multiph. Flow **37**, 149 (2011).
[63] L. Tian, Y. Xu, J. G. M. Kuerten, and J. J. W. van der Vegt, An h-adaptive local discontinuous Galerkin method for the Navier-Stokes-Korteweg equations, J. Comput. Phys. **319**, 242 (2016).
[64] W. Mickel, L. Joly, and T. Biben, Transport, phase transitions, and wetting in micro/nanochannels: A phase field/DDFT approach, J. Chem. Phys. **134**, 094105 (2011).
[65] J. Liu, C. M. Landis, H. Gomez, and T. J. R. Hughes, Functional entropy variables: A new methodology for deriving thermodynamically consistent algorithms for complex fluids, with particular reference to the isothermal Navier-Stokes-Korteweg equations, J. Comput. Phys. **248**, 47 (2013).
[66] A. Pecenko, J. G. M. Kuerten, and C. W. M. van der Geld, A diffuse-interface approach to two-phase isothermal flow of a van der Waals fluid near the critical point, Int. J. Multiph. Flow **36**, 558 (2010).
[67] A. Onuki, Dynamic van der Waals theory, Phys. Rev. E **75**, 036304 (2007).
[68] F. Magaletti, L. Marino, and C. M. Casciola, Shock Wave Formation in the Collapse of a Vapor Nanobubble, Phys. Rev. Lett. **114**, 064501 (2015).
[69] P. Yue, C. Zhou, and J. J. Feng, Spontaneous shrinkage of drops and mass conservation in phase-field simulations, J. Comput. Phys. **223**, 1 (2007).
[70] J. Neusser, C. Rohde, and V. Schleper, Relaxation of the Navier-Stokes-Korteweg equations for compressible two-phase flow with phase transition, Int. J. Numer. Meth. Fluids **79**, 615 (2015).
[71] J. Bueno, C. Bona-Casas, Y. Bazilevs, and H. Gomez, Interaction of complex fluids and solids: Theory, algorithms and application to phase-change-driven implosion, Comput. Mech. **55**, 1105 (2015).
[72] Z. Qiao and S. Sun, Two-phase fluid simulation using a diffuse interface model with Peng-Robinson equation of state, SIAM J. Sci. Comput. **36**, B708 (2014).
[73] J. Kou and S. Sun, Multi-scale diffuse interface modeling of multi-component two-phase flow with partial miscibility, J. Comput. Phys. **318**, 349 (2016).
[74] P. Papatzacos, A model for multiphase and multicomponent flow in porous media, built on the diffuse-interface assumption, Transp. Porous Med. **82**, 443 (2010).
[75] P. Papatzacos and S. M. Skjaeveland, Diffuse-interface modeling of two-phase flow for a one-component fluid in a porous medium, Transp. Porous Med. **65**, 213 (2006).
[76] X. Fu, L. Cueto-Felgueroso, and R. Juanes, Thermodynamic coarsening in partially-miscible binary mixtures arrested by viscous fingering, Phys. Rev. E **94**, 033111 (2016).
[77] F. Moebius, D. Canone, and D. Or, Characteristics of acoustic emissions induced by fluid front displacement in porous media, Water Resour. Res. **48**, W11507 (2012).
[78] F. Moebius and D. Or, Interfacial jumps and pressure bursts during fluid displacement in interacting irregular capillaries, J. Colloid Interface Sci. **377**, 406 (2012).
[79] N. Shokri, M. Sahimi, and D. Or, Morphology, propagation dynamics and scaling characteristics of drying fronts in porous media, Geophys. Res. Lett. **39**, L09401 (2012).

[80] K. J. Måløy, L. Furuberg, J. Feder, and T. Jøssang, Dynamics of Slow Drainage in Porous Media, Phys. Rev. Lett. **68**, 2161 (1992).
[81] L. Furuberg, K. J. Måløy, and J. Feder, Intermittent behavior in slow drainage, Phys. Rev. E **53**, 966 (1996).
[82] E. Aker, K. J. Måløy, A. Hansen, and S. Basak, Burst dynamics during drainage displacements in porous media: Simulations and experiments, Europhys. Lett. **51**, 55 (2000).
[83] M. Prat, Percolation model of drying under isothermal conditions in porous media, Int. J. Multiph. Flow **19**, 691 (1993).
[84] M. Prat, Recent advances in pore-scale models for drying of porous media, Chem. Eng. J. **86**, 153 (2002).
[85] E. Shahraeeni and D. Or, Pore-scale analysis of evaporation and condensation dynamics in porous media, Langmuir **26**, 13924 (2010).
[86] N. Shokri, P. Lehmann, P. Vontobel, and D. Or, Drying front and water content dynamics during evaporation from sand delineated by neutron radiography, Water Resour. Res. **44**, W06418 (2008).
[87] N. Shokri, P. Lehmann, and D. Or, Evaporation from layered porous media, J. Geophys. Res. **115**, B06204 (2010).
[88] S. Dong, On imposing dynamic contact-angle boundary conditions for wall-bounded liquid-gas flows, Comput. Meth. Appl. Mech. Eng. **247–248**, 179 (2012).
[89] K. Glasner, A diffuse-interface approach to Hele-Shaw flow, Nonlinearity **16**, 49 (2003).
[90] W. Dreyer, J. Giesselmann, C. Kraus, and C. Rohde, Asymptotic analysis for Korteweg models, Interfaces Free Bound. **14**, 105 (2012).
[91] H. H. Hu and D. D. Joseph, Miscible displacement in a Hele-Shaw cell, Z. Angew Math. Phys. **43**, 626 (1992).
[92] H. Davis, in *Proceedings of the Symposium on Numerical Simulation in Oil Recovery on Numerical Simulation in Oil Recovery, Minneapolis, 1987*, edited by M. F. Wheeler (ACM, New York, 1988), p. 105.
[93] D. Joseph, A. Huang, and H. Hu, Non-solenoidal velocity effects and Korteweg stresses in simple mixtures of incompressible liquids, Physica D **97**, 104 (1996).
[94] C.-Y. Chen and E. Meiburg, Miscible displacements in a capillary tube. Part 2. Numerical simulations, J. Fluid Mech. **326**, 57 (1996).
[95] C.-Y. Chen, L. Wang, and E. Meiburg, Miscible droplets in a porous medium and the effects of Korteweg stresses, Phys. Fluids **13**, 2447 (2001).
[96] C.-Y. Chen and E. Meiburg, Miscible displacements in capillary tubes: Influence of Korteweg stresses and divergence effects, Phys. Fluids **14**, 2447 (2002).
[97] V. Joekar-Niasar, F. Doster, R. T. Armstrong, D. Wildenschild, and M. A. Celia, Trapping and hysteresis in two-phase flow in porous media: A pore-network study, Water Resour. Res. **49**, 4244 (2013).
[98] V. Joekar-Niasar, S. M. Hassanizadeh, and A. Leijnse, Insights into the relationships among capillary pressure, saturation, interfacial area and relative permeability using pore-network modeling, Transp. Porous Med. **74**, 201 (2008).
[99] See Supplemental Material at http://link.aps.org/supplemental/10.1103/PhysRevFluids.3.084302 for videos 1 and 2.
[100] G. Tryggvason and H. Aref, Numerical experiments on Hele Shaw flow with a sharp interface, J. Fluid Mech. **136**, 1 (1983).
[101] A. Lindner, P. Coussot, and D. Bonn, Viscous Fingering in a Yield Stress Fluid, Phys. Rev. Lett. **85**, 314 (2000).
[102] A. Lindner, D. Bonn, E. Poiré Corvera, M. Ben Amar, and J. Meunier, Viscous fingering in non-Newtonian fluids, J. Fluid Mech. **469**, 237 (2002).
[103] S. Nguyen, R. Folch, V. K. Verma, H. Henry, and M. Plapp, Phase-field simulations of viscous fingering in shear-thinning fluids, Phys. Fluids **22**, 103102 (2010).
[104] S. Li, J. S. Lowengrub, J. Fontana, and P. Palffy-Muhoray, Control of Viscous Fingering Patterns in a Radial Hele-Shaw Cell, Phys. Rev. Lett. **102**, 174501 (2009).
[105] T. T. Al-Housseiny, P. A. Tsai, and H. A. Stone, Control of interfacial instabilities using flow geometry, Nat. Phys. **8**, 747 (2012).

[106] D. Pihler-Puzović, P. Illien, M. Heil, and A. Juel, Suppression of Complex Fingerlike Patterns at the Interface between Air and a Viscous Fluid by Elastic Membranes, Phys. Rev. Lett. **108**, 074502 (2012).
[107] P. Concus and R. Finn, On the behavior of a capillary surface in a wedge, Proc. Natl. Acad. Sci. U.S.A. **63**, 292 (1969).
[108] T. C. Ransohoff and C. J. Radke, Laminar flow of a wetting liquid along the corners of a predominantly gas-occupied noncircular pore, J. Colloid Interface Sci. **121**, 392 (1988).
[109] M. Dong and I. Chatzis, The imbibition and flow of a wetting liquid along the corners of a square capillary tube, J. Colloid Interface Sci. **172**, 278 (1995).
[110] L. A. Romero and F. G. Yost, Flow in an open channel capillary, J. Fluid Mech. **322**, 109 (1996).
[111] M. M. Weislogel and S. Lichter, Capillary flow in an interior corner, J. Fluid Mech. **373**, 349 (1998).
[112] J. Bico and D. Quéré, Rise of liquids and bubbles in angular capillary tubes, J. Colloid Interface Sci. **247**, 162 (2002).
[113] B. Zhao, C. W. MacMinn, and R. Juanes, Wettability control on multiphase flow in patterned microfluidics, Proc. Natl. Acad. Sci. U.S.A. **113**, 10251 (2016).
[114] C. Odier, B. Levaché, E. Santanach-Carreras, and D. Bartolo, Forced Imbibition in Porous Media: A Fourfold Scenario, Phys. Rev. Lett. **119**, 208005 (2017).
[115] F. Chauvet, P. Duru, S. Geoffroy, and M. Prat, Three Periods of Drying of a Single Square Capillary Tube, Phys. Rev. Lett. **103**, 124502 (2009).
[116] L. Xu, S. Davies, A. B. Schofield, and D. A. Weitz, Dynamics of Drying in 3D Porous Media, Phys. Rev. Lett. **101**, 094502 (2008).
[117] F. Moebius and D. Or, Pore scale dynamics underlying the motion of drainage fronts in porous media, Water Resour. Res. **50**, 8441 (2014).
[118] S. Berg, H. Ott, S. A. Klapp, A. Schwing, R. Neiteler, N. Brussee, A. Makurat, L. Leu, F. Enzmann, J. Schwarz, M. Kersten, S. Irvine, and M. Stampanoni, Real-time 3D imaging of haines jumps in porous media flow, Proc. Natl. Acad. Sci. U.S.A. **110**, 3755 (2013).
[119] P. Fantinel, O. Borgman, R. Holtzman, and L. Goehring, Drying in a microfluidic chip: Experiments and simulations, Sci. Rep. **7**, 15572 (2017).
[120] D. Or, P. Lehmann, E. Shahraeeni, and N. Shokri, Advances in soil evaporation physics: A review, Vadose Zone J. **12**, 1 (2013).
[121] C. M. Cejas, J.-C. Castaing, L. Hough, C. Frétigny, and R. Dreyfus, Experimental investigation of water distribution in a two-phase zone during gravity-dominated evaporation, Phys. Rev. E **96**, 062908 (2017).